GEORG-AUGUST-UNIVERSITÄT
GÖTTINGEN

Fakultät für
Physik

Bachelor's Thesis

Modellierung der ITk Services in der Crack Barrel Region

Modelling of ITk Services in the Crack Barrel Region

prepared by

Luke Selzer

from Kassel

at the II. Physikalischen Institut

Thesis number:	II.Physik-UniGö-BSc-2026/03
Thesis period:	7th November 2025 until 2nd March 2026
First referee:	Prof. Dr. Stan Lai
Second referee:	apl. Prof. Dr. Jörn Große-Knetter

Abstract

With the High Luminosity LHC upgrade planned to be completed in 2030, preparations at the ATLAS experiment of both software and hardware upgrades are being done. The most significant upgrade is the new inner tracking detector (ITk) which will greatly improve the precision of the physics analysis.

This thesis is about the modelling of material in the Crack Barrel Region, one of the last missing parts in the geometry model of the ITk. The model is implemented with GeoModelXML and is based on two technical CAD models which contain the geometry of the Crack Barrel Region in different complexity. As a replacement for the currently used model which is outdated, the implementation of the model shown in this thesis will be used in the Geant4 based physics simulation of the ATLAS experiment. Simulated events of the ATLAS experiment including updated geometry are essential for comparison with experimental data collected in Run 4 of the LHC to test the theoretical predictions of the Standard Model and to search for new physics.

Contents

1. Introduction

Human interest in new discoveries is a constant driving force of mankind. It is this curiosity that sparked not only the search for existence outside of our planet but also the longing to understand the most basic building blocks of the matter that forms everything surrounding us. The first steps were taken by Democritus in 400 B.C. who first postulated that there needs to be a smallest, indivisible kind of matter that serves as a building block for more complex structures. In the 19th century the scientific description of such particles started to take shape with the first description of atoms which at that time were the smallest building blocks known to man.

The discovery of subatomic particles in the second half of the 20th century however gave rise to an even deeper understanding of matter, which is described today by the Standard Model of Particle Physics (SM) [1–7]. This model provides the most fundamental description of the world around us as of today. Many experiments are consistent with the predictions of the SM but there is also strong experimental evidence that the SM is not a complete theory of nature. Thus, there are new theories emerging that include Beyond Standard Model Physics (BSM) [8, 9].

In order to test any model, the first question to be asked is "What do we expect to happen?" which is then followed by the experiment which gives an answer to the question "What do we observe?". It is the difference of the answers to these questions that is most important to fundamental research as it drives the process of iterating over model correction and comparison with the experiment. The first question proves to be very difficult to answer because the prediction concentrates on the experiment, not theoretical processes and because of that the experimental setup has to be considered. Experiments in particle physics however are very complicated, which motivates the need of computer simulations in order to correctly interpret experimental measurements based on the current physics theory.

This thesis deals with the challenge of modelling components of the ATLAS detector

located at CERN in Geneva [10, 11]. More specifically, the new Inner Tracker (ITk) that will be the new tracking detector of the experiment, is of interest in this thesis [12]. These modelled components are then supplied to the simulation as an improvement of the current description that is used in the simulation for the ATLAS experiment. The structure of this thesis is as follows. Chapter 2 gives an overview of the SM as well as the modelling and simulation of particle physics experiments. Chapter 3 deals with the experimental setup at the Large Hadron Collider (LHC) at CERN as well as the ATLAS experiment which forms the basis of this work. The upgrade of the LHC [13] is also discussed here as it provides motivation for the new model as well as the upgrade of the ATLAS experiment. In Chapter 4, the details in the Crack Barrel Region (CBR) of the ITk and their implementation are discussed. Chapter 5 then gives a visual comparison of the created model with the provided technical CAD model. Chapter 6 gives a conclusion as well as an outlook over which improvements can be made and what the next steps are.

2. Theoretical Background

In order to correctly describe the ITk Crack Barrel Region, the physical processes that are the basis of the interaction of high energy particles with detector material first need to be understood. This chapter provides the necessary theoretical background to understand the necessity of simulations in particle physics, as well as the considerations that need to be taken into account before a detector model can be implemented. For the description of material interactions inside the detector it is necessary to first know all of the fundamental particles and interactions described by the SM, to then highlight specific interactions that are important for the correct implementation of a detector model.

2.1. The Standard Model of Particle Physics

The Standard Model of particle physics [1–7] has evolved to become the most detailed and established theory of nature for fundamental particles and interactions. Experimental tests and theoretical research are performed worldwide and make it the most trusted theory that humanity has come up with for the description of fundamental physics. Even though it is not a complete description of nature, it is the best there currently is, and therefore forms the basis of current research in particle physics.

The fundamental particles

The Standard Model of Particle Physics (SM) contains all known fundamental particles and interactions except gravity as well as their interactions [1–7]. It comprises twelve fundamental particles and their corresponding antiparticles as well as four exchange bosons that mediate interactions between different particles. In addition to that there is also the Higgs boson which interacts with the particles through the Higgs mechanism. These particles are shown in Fig. 2.1.

The fundamental particles consist of two groups of six fermions - the quarks and the leptons. These differ in the interactions they take part in and in the charges they possess. They further contain three generations of particles which form pairs that have interesting

symmetries in their properties. Fermions all have a spin of $S = \frac{1}{2}$ and each is identified with a distinct rest mass. The generations of fermions can be seen in Fig.2.1.

Starting with the leptons, the first generation is made up of the negatively charged electron and a neutral electron neutrino. They differ not only in their electric charge but also in their masses, as the electron mass is $m_e \approx 0.511$ MeV [14] whereas the electron neutrino mass is $m_{\nu_e} < 1$ eV [14]. These differences are very useful when trying to distinguish the particles in the detector. In the case of the neutrino, the combination of not possessing charge and also only interacting weakly with matter makes it very difficult to detect.

The second generation leptons are called muon and muon neutrino, and only differ from their first generation counterparts in terms of mass with the muon mass being $m_\mu \approx 105.66$ MeV [14]. For the muon neutrino the mass is $m_{\nu_\mu} < 0.17$ MeV [14]. The larger mass of the muon causes it to decay rapidly into the stable electrons.

Tau leptons have a mass of $m_\tau \approx 1.78$ GeV [14] and the tau neutrino possesses a mass of $m_{\nu_\tau} < 18.2$ MeV [14]. The third and final generation of leptons is even more difficult to identify as the tau leptons decay into various final states.

For the quarks, the grouping into generations pairs one up type-quark with a down-type quark as visualised in Fig.2.1. The up-type quarks consist of the up (u), charm (c) and the top (t) quark, and each type carries an electric charge of $Q_u = +\frac{2}{3}e$. For each of these three generations of up-type quarks, there is down-type quark which are the down (d), strange (s) and bottom (b) quark, respectively. These carry an electric charge of $Q_u = -\frac{1}{3}e$. In addition to the electric charge, the quarks also possess a colour charge which can be either red, green or blue. This special charge corresponds to the strong interaction that is exclusively relevant for the quarks and the mediating bosons of the interaction, which are the gluons. The differences in mass that are manifest in the lepton generations hold for quarks as well. In general, lifetimes for higher generations become shorter due to their larger masses. The top quark mass of $m_t \approx 172.57$ GeV [14] is two orders of magnitude larger than the bottom quarks mass of $m_b \approx 4.18$ GeV [14]. Additionally the decay of quarks into quarks that do not belong to the same generation is suppressed as shown in the quark mixing theory [16]. For this reason, the lifetime of the bottom quark is magnitudes larger than the lifetime of all of the other quarks, which can be used to distinguish it from other quarks.

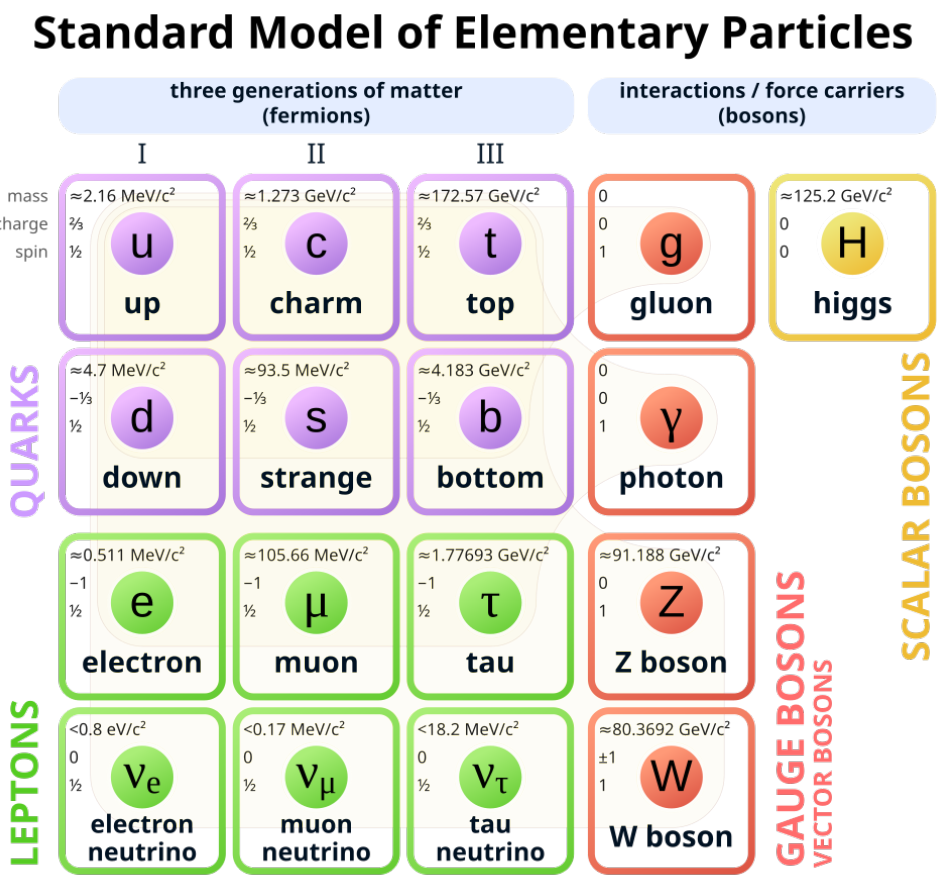

Figure 2.1.: The Standard Model of particle physics with the six quarks in purple, the six leptons in green and the gauge bosons in orange. The scalar Higgs boson is shown in yellow. Every particle is indexed on the top left with its mass m, electric charge Q and spin S [15].

All of the particles mentioned above have a corresponding antiparticle that is identical to the normal particle but carries the opposite charges.

The fundamental interactions

Interactions of particles are responsible for complex structures that make up the world that we observe. The three fundamental interactions that are described by the SM are electromagnetic interactions, strong interactions and weak interactions. These interactions all have an underlying quantum field theory that describes the quantum mechanical processes involved. These theories are called Quantum Electrodynamics (QED) for the electromagnetic interaction and Quantum Chromodynamics (QCD) for the strong interaction. The weak interactions are described together with the electromagnetic interactions in a unified electroweak theory.

The electromagnetic interaction is mediated by a gauge boson that is called the photon γ, with spin S = 1. This photon couples to the electric charge of particles Q, and therefore all fundamental particles with an electric charge can interact electromagnetically [3]. The photon is not charged at all and therefore not able to interact with other photons at leading order. Photons are also massless and therefore able to mediate force regardless of the total energy of the initial and final state particles as long as energy is conserved between these states.

Weak interactions are mediated by the $W^{\pm}$ and the Z^0 vector bosons that carry their electric charges of $\pm$ 1 and 0 respectively. At high energy scales of $\approx$ 246 GeV the electromagnetic interaction and weak interaction are combined in what is known as electroweak unification [1, 2]. The bosons couple to all charged particles, with the Z^0 boson being able to couple to neutrinos too. The W mass is $m_W \approx 80.376(33)$ GeV [14] and the Z^0 mass is $m_Z \approx 91.1876(21)$ GeV [14] which is especially important for interactions that take place at this energy scale.

Gluons mediate the strong interaction. There are eight gluons in total and they differ in their colour charges. Gluons couple to the colour charges of quarks [7]. Because the gluons carry the charge of their interaction themselves, they interact with other gluons. Furthermore they carry a colour and an anticolour and are therefore bound by colour confinement, like the quarks. Colour confinement states that free particles can only exist with neutralized colour [17]. This leads to the formation of bound quark states with either all three colours that are called baryons or all anticolours that are called antibaryons. The other possible bound states are mesons that are made up out of two quarks with colour and corresponding anticolour [7]. High energy quarks and gluons that are created in an interaction hadronize in jets of particles to form the bound states explained above.

The Higgs boson is a scalar boson with spin S = 0 [5, 6]. It is an excitation of the Higgs field which has a vacuum expectation value of $\approx$ 246 GeV. Through the Higgs mechanism, this Higgs field couples to all particles with a coupling strength proportional to the particles mass. In addition to this the Higgs boson carries a mass of $m_H \approx 125.11$ GeV [18], and it can self-couple to other Higgs bosons.

All of the aforementioned interactions can be visualised by Feynman diagrams which represent different interactions and particles with different lines. Feynman diagram ex-

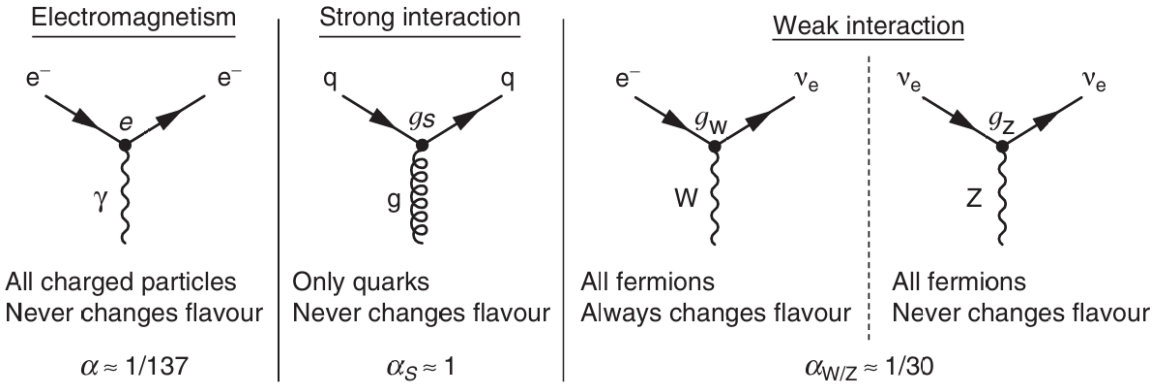

Figure 2.2.: Feynman diagrams for the interaction vertices of the three fundamental forces and their gauge bosons. [19]

amples for the three fundamental interactions are shown in Figure 2.2.

2.2. Particle interactions with matter

The design of particle physics experiments needs to take into account how particles interact with matter. These interactions play a crucial role in how a particle physics detector is created, both for the active material that is used to detect these interactions, as well as the passive material of support structures and services. As explained in Section 2.1, different particles interact differently with matter and not all interactions are relevant for every particle. Electromagnetic interactions are relevant for all electrically charged particles whereas strong interactions can only occur between particles that carry colour charge such as quarks and gluons. These interactions are characterised by a material dependent mean free path λ [20]

$$\lambda = \frac{1}{N \cdot \sigma} \tag{2.1}$$

which describes the statistical travel length of a particle in the material until an interaction with the material occurs. N describes the atomic density and σ describes the cross section of the relevant interaction process. The cross section for material interactions is generally a function of the atomic number Z, the mass number A and the energy E of the incoming particle. Further calculations depend heavily on the interactions and particles involved [20].

When characterizing material interactions, it is important to distinguish between the interactions of photons and the interactions of charged particles. Photons can cause

electron-positron pair production inside an electric field of a nucleus which leads to more particles that interact further with the material. Pair production is the dominant process in which photons interact with matter above energies of the MeV scale, which is the case inside the ATLAS experiment. In this process, the cross section σ scales approximately with Z^2, which implies that much more pair production occurs in materials with higher atomic numbers. It is also possible for the photon to release only a part of its energy and be scattered in a process called Compton scattering, where σ scales only with Z. Compton scattering however is less dominant at higher energies of MeV and above. The last relevant photon interaction with matter is the photoelectric effect. This effect describes the release of loosely bound electrons in the atomic outer shells by collision with an incoming photon. This is also less dominant than the pair production at higher energies, but can cause permanent damage in both active materials and electrical signal transmission.

The Bethe-Bloch function describes the interaction and energy loss of all charged particles more massive than the electron, but it does not give accurate predictions for electrons because they cannot be distinguished from the valence electrons after the collision. Another reason for the failure of the Bethe-Bloch function to predict electron energy loss in matter is the fact that electrons lose energy in matter dominantly through the effect of Bremsstrahlung which the Bethe-Bloch function does not cover. Bremsstrahlung is the process of electrons deflecting in the positive electric field of a nucleus and emitting a photon. This is not possible in the absence of matter because the nucleus is needed to catch the recoil of the electron deflection or else momentum conservation would not be fulfilled.

For heavier charged particles, the energy loss is described by the Bethe-Bloch function which includes many small corrections and effects that describe interactions with the charged fields of nuclei in matter. It is described as

$$-\frac{dE}{dx} = \frac{4\pi n Z^2}{m_e c^2 \beta^2} \left(\frac{e^2}{4\pi\epsilon_0}\right)^2 \left[\ln\left(\frac{2m_e c^2 \beta^2}{I(1-\beta^2)}\right) - \beta^2\right] \tag{2.2}$$

with n being the electron density of the material, Z the charge of the incoming par-

ticle in units of e and m_e being the electron mass. Furthermore c is describing the speed of light in vacuum, β is the relativistic speed of the incoming particle, and ϵ_0 is the electric field constant. I is a material specific constant that increases linearly with increasing atomic number. The Z-dependence is of second order which shows that a higher charge of the incoming particle translates into a greater energy loss in the medium. Additionally the energy loss has a minimum at the range of $\beta\gamma = 3$ to 4 which defines the minimal ionizing particles (MIPs) and is only loosely dependent on the material. This results for example in the case of muons penetrating copper in Fig. 2.3.

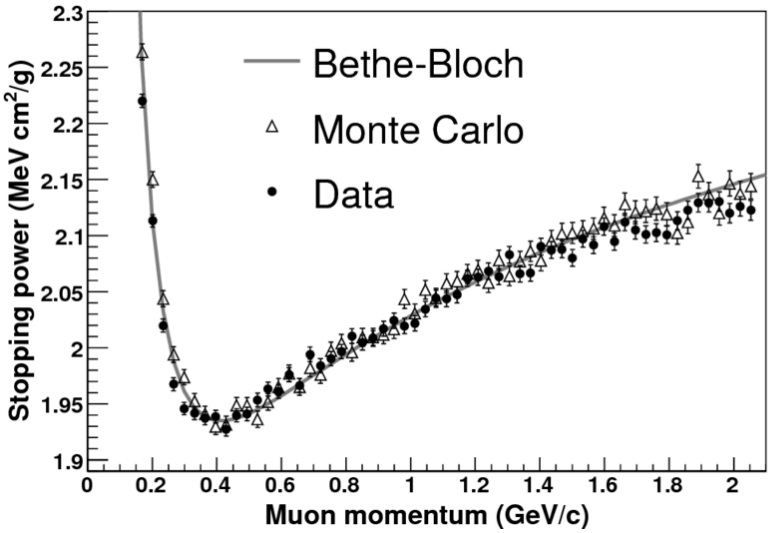

Figure 2.3.: The Bethe-Bloch curve for muons traversing copper as for example in the scintillators of the ECAL. The Bethe-Bloch curve looks similar for all charged particles heavier than the electron. [21]

The interactions included in the Bethe-Bloch function are those of highly energetic charged particles that collide with valence electrons of atoms in the material. This leads to the electrons either being ejected from the outer shells of the atom which is called ionization or the electron gaining energy and remaining bound to the atom in an excited state. Both processes are inelastic scatterings that lead to energy loss and change of the direction of flight of the incoming particle. In the tracking detector, this enables the recreation of particle tracks because the particle does not get stopped by the material detecting it.

Additionally to singular interactions, the effect of multiple scattering has to be taken into account. Multiple scattering describes the above mentioned particle interactions sta-

tistically for a given distance traversed in the medium because singular interactions with the material only describe insignificant energy depositions in the material. This effect leads to charged particles changing their direction of movement as well as reducing their energy for a given distance. Many interactions are needed to make a significant impact on the traversing particles speed and direction.

2.3. Simulation in Particle Physics

Geant4 based Simulation

The simulations of particle physics experiments are performed with Geant4, a software toolkit developed and maintained by the international Geant4 collaboration [22]. Geant4 is an object oriented C++ based toolkit for Monte Carlo simulation which is tuned to be as fast as possible. Monte Carlo simulation describes the process of random testing to obtain a statistical overview over a complex problem [22]. Simulated events can be analyzed on multiple different physical properties such as trajectories and interactions of the involved particles. The basis of the simulation is given by geometry modelled with GeoModelXML [23] which is described in the next section. This is the part that I have worked on. The simulation of interactions of particles with the material is based on the physical predictions of the SM and simulated data is generated as close to the experimental conditions as possible. For this reason, the geometry defined with GeoModelXML has to be as realistic as possible, both in the exact position and volume as well as the material composition of the detector. This leads to an optimization between having the model be precise enough to generate a simulation that is sufficiently in agreement with true data while keeping the model as simple as possible.

GeoModelXML based Modelling

GeoModelXML is an XML based toolkit that was designed at CERN to describe detector geometry for simulation [23]. The geometry is implemented inside XML files and is based on predefined objects that are characterised by the necessary parameters. A shape is the most basic object and can be one of many predefined ones such as boxes, tubes or cones. An alternative for more complex shapes is a boolean solid comprised of many such shapes. The boolean solid can be either a subtraction, intersection or union of shapes for which examples are shown in Fig. 2.4 and 2.5. A subtraction takes two shapes and subtracts the second from the first in the volume of intersection of the two shapes. The intersection of two shapes gives the intersecting volume of two shapes. Lastly the union of two shapes

yields the combined volume of two shapes, including the intersection. Although boolean solids seem to be the preferred choice of implementation because they offer infinite possibilities, they are not. A shape constructed out of a boolean solid in GeoModelXML leads to a higher processing power needed in the simulation compared to a similar shape constructed without the use of boolean solids. Boolean solids should therefore be avoided as much as possible. It is important to note that these shapes are not physical objects yet because this requires material definition.

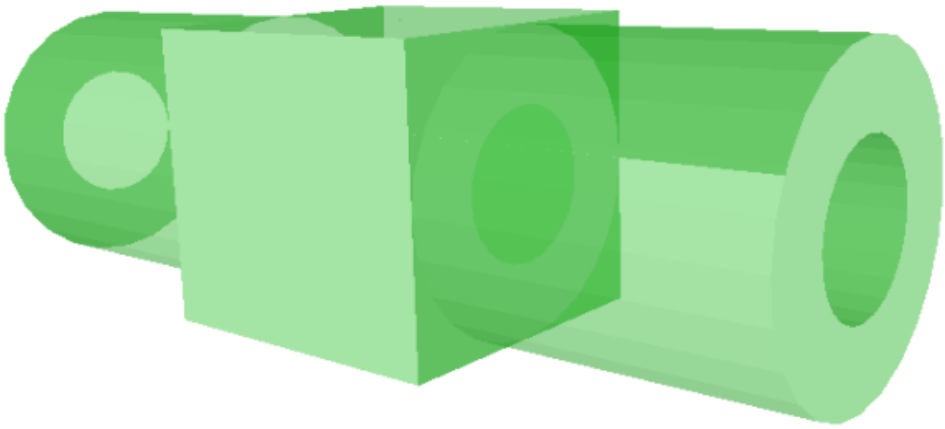

Figure 2.4.: An example of a union of two shapes to form a boolean solid is shown. The two shapes are a box and a tube. Together as a union, they form a singular coherent volume with no overlapping parts.

Shapes then are referenced in the creation of logical volumes (logvol) that need a shape and a material, as well as a name to reference them. These logvols are now objects that can interact and as such show up in the model they are implemented in. Defined logvols can now be copied and moved inside the space where they serve as their real experiment counterpart. It is important to note that all logvols have a flag that marks them as either sensitive or not sensitive. This flag filters out all logvols that need their material interactions converted into simulated data which correspond to active materials in the real experiment, for example the silicon layer of pixels or strips. Non-sensitive materials are structural components, as well as cables and pipes. All of the volumes covered in the CBR will be flagged as non-sensitive. To better organize these logvols, assemblies are used to combine them into groups that can be referenced and copied as one object. These

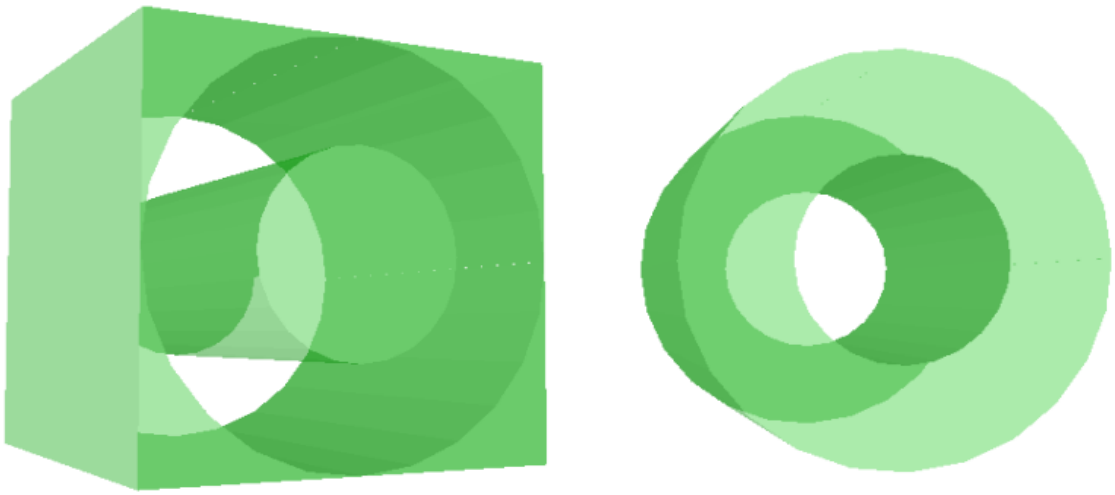

Figure 2.5.: Two examples of boolean solids are shown. On the left there is a subtraction of a box with a tube, leaving a hollowed out box with a smaller tube in the middle. On the right there is an intersection of the same box and tube, leaving only the volume that is present in both the box and the tube.

assemblies do not need a predefined shape as part of their definition and also do not take part in the simulation as they do not have any material themselves. It is also possible to collect multiple logvols into a single logvol containing the daughter volumes without overlap. Creating more layers than necessary for structuring is to be avoided, because the more branches of the tree of assemblies and logvols the simulation interpreter needs to search for actual geometry, the longer it takes for the simulation to run.

In order to visualize the implemented geometry, GeoModelXML comes with a tool called GeoModelVisualisation (gmex). An example of the interface is given in Fig. A.1. The visualisation comes with a lot of tools that include individual visualisation of sub volumina, local and global coordinate systems as well as detailed material information and colour coding options. The model can be rotated freely and the transparency of different parts can be adjusted as well.

Another useful tool provided with the GeoModelXML toolkit is called GeoModelClash (gmclash) which serves the purpose of checking the implemented geometry for overlapping volumes. These would be non-physical and are suboptimal for the simulation. For this reason gmclash is an essential tool to check that the implemented model is valid. Clash checks are done with random samples of two volumes and if a clash is found, the search for these two volumes is aborted. The output of this tool comes in form of a .json file

which describes the clashed volumes with their names and relation as well as the position of the clash. These files can also be read into gmex which can display clash points over the corresponding geometry which makes troubleshooting a lot easier. The relation of the clash is important for characterization of the underlying errors in implementation and are therefore colour coded differently. An example of such a clash would be two boxes overlapping with a clash in the overlap area. The output file of gmclash checking this geometry lists a clash as an overlap of the boxes with position, involved volumes and that the volumes were on the same level of the geometry tree (named a sister-sister clash). This output file can be read into the visualisation to show the clashes inside the model as shown in Fig. 2.6.

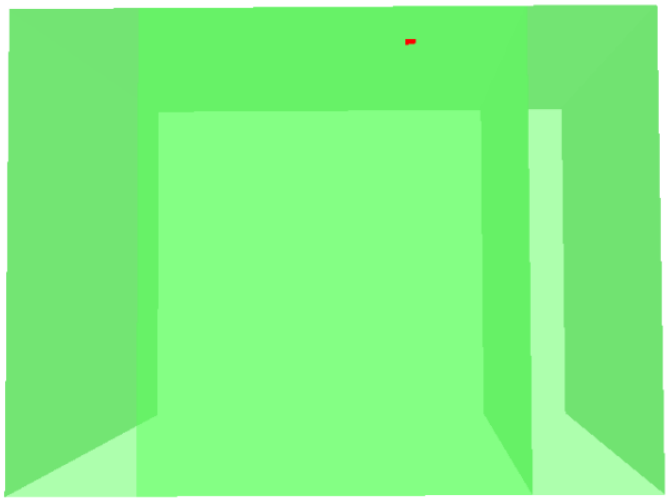

Figure 2.6.: An example of two boxes with a clear overlap in the middle is shown. The output of gmclash is visualised as a red point. The description in the output file links the point to the two volumes.

GeoModelStatistics (gmstatistics) is another tool that was used for the implementations done in this thesis. This tool serves as a check on the memory occupancy of the given geometry which is correlated with the performance of the simulation its used in as loading more data consequently leads to longer simulation times. Using this tool yields a precise estimate of the quality of implementation, especially if compared to similar geometries and different implementations of the same geometry.

3. The ATLAS Experiment at CERN

The ATLAS experiment [11] at CERN [10] is the basis for the work discussed in this thesis. The goal is to implement a GeoModelXML based model of the Crack Barrel Region. Since the Crack Barrel Region is part of the new tracking detector of the ATLAS experiment, it is important to understand the experimental setup at CERN as well as the ATLAS experiment. The next chapter will give an overview of the experimental possibilities and restrictions of the ATLAS experiment at CERN as well as the upgrades of the HL-LHC [13] and the new Inner Tracker (ITk) [12].

3.1. The Large Hadron Collider

The Large Hadron Collider (LHC) is the largest particle accelerator in the world, producing an instantaneous luminosity of $\mathcal{L}= 10^{34}$ cm^{-2}s^{-1} [10] with a centre-of-mass energy of $\sqrt{s} = 13.6$ TeV [10]. This is achieved by accelerating proton bunches in five different stages to then collide them inside one of the four stationed experiments ATLAS, CMS, LHCb or ALICE. These facilities are located at CERN in Geneva, Switzerland.

As shown in Fig.3.1, the first step of producing high energy protons in this facility is accelerating H^- ions in the linear accelerator (LINAC 4) to an energy of about 160 MeV [25]. These ions are converted to protons by removing the two electrons. Further injection into the Proton Synchrotron Booster (PSB) leaves the protons with an energy of 2 GeV. This serves as a booster for the Proton Synchrotron (PS) that ejects the protons with 26 GeV into the Super Proton Synchrotron (SPS) which accelerates them to 450 GeV. After this step the protons enter the LHC in opposing directions to be accelerated further on the 27 km long track to their final centre-of-mass energy of $\sqrt{s} = 13.6$ TeV [25]. The acceleration steps are performed on bunches of about 10^{11} protons for higher luminosities and easier acceleration [25]. These bunches of opposite rotation in the LHC collide in one of the experiments and the collisions then can be analyzed via electronic readout.

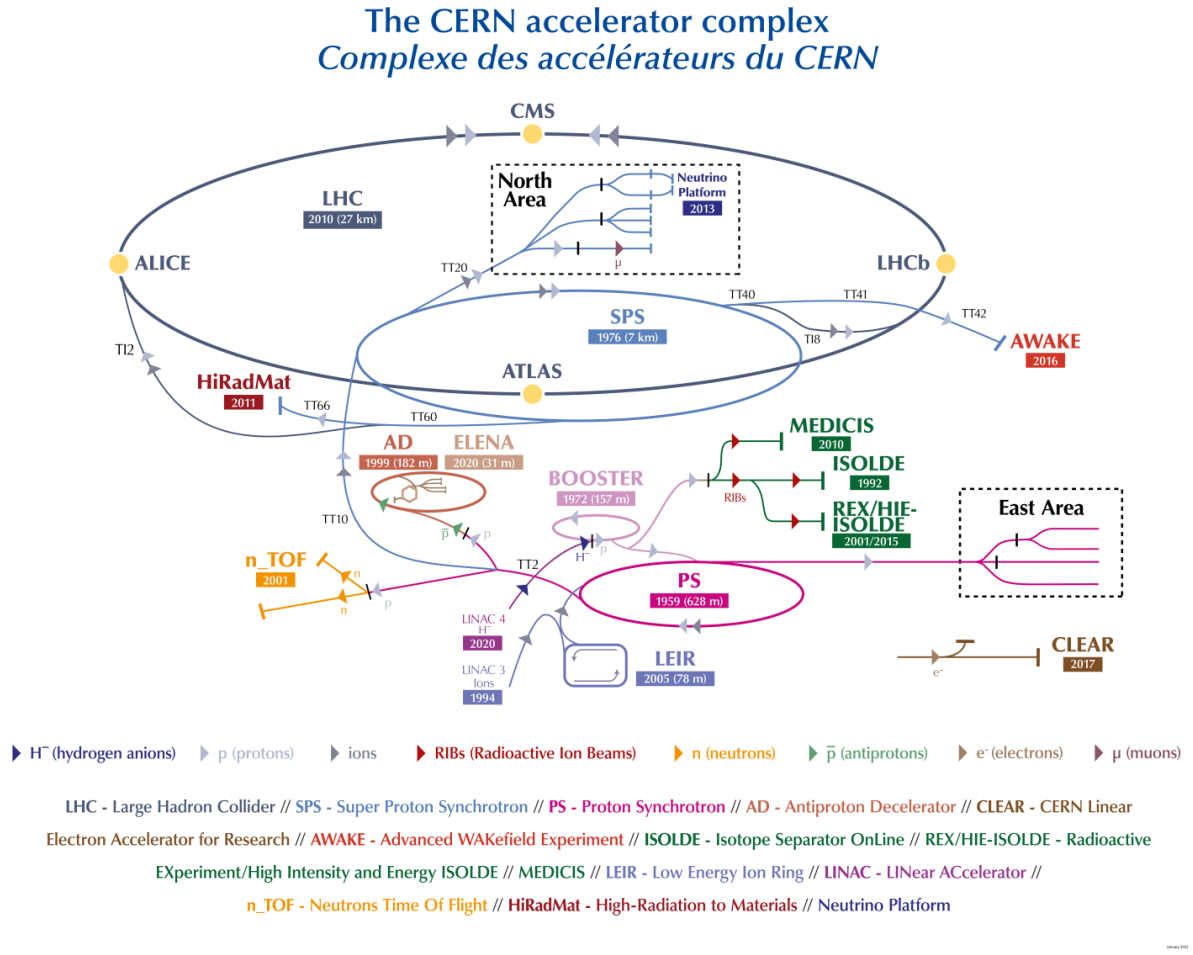

Figure 3.1.: Schematic of the CERN accelerator system with the LINAC, PSB, PS, SPS and finally the LHC accelerator [24].

3.2. The ATLAS Experiment

The ATLAS detector is one of the two all-purpose experiments at the LHC at CERN, the other being CMS [26]. As the largest of the detectors, it is 25 m in height and 44 m in length with a weight of approximately 7000 tonnes. The entire system is forward-backward symmetric and consists of multiple subsystems that all serve specific purposes [11]. The visualisation in Fig.3.2 shows the different subsystems and their distribution into the barrel parts and the end caps.

Starting with the innermost segment, the Inner Detector (ID) consists of a four layer pixel detector, the semiconductor tracker (SCT) and the transition radiation tracker (TRT). The pixel detector layers are positioned so that they completely cover all possible paths of a particle up to a pseudorapidity of $|\eta| \leq 2.5$ [11]. This pseudorapidity gives a measure

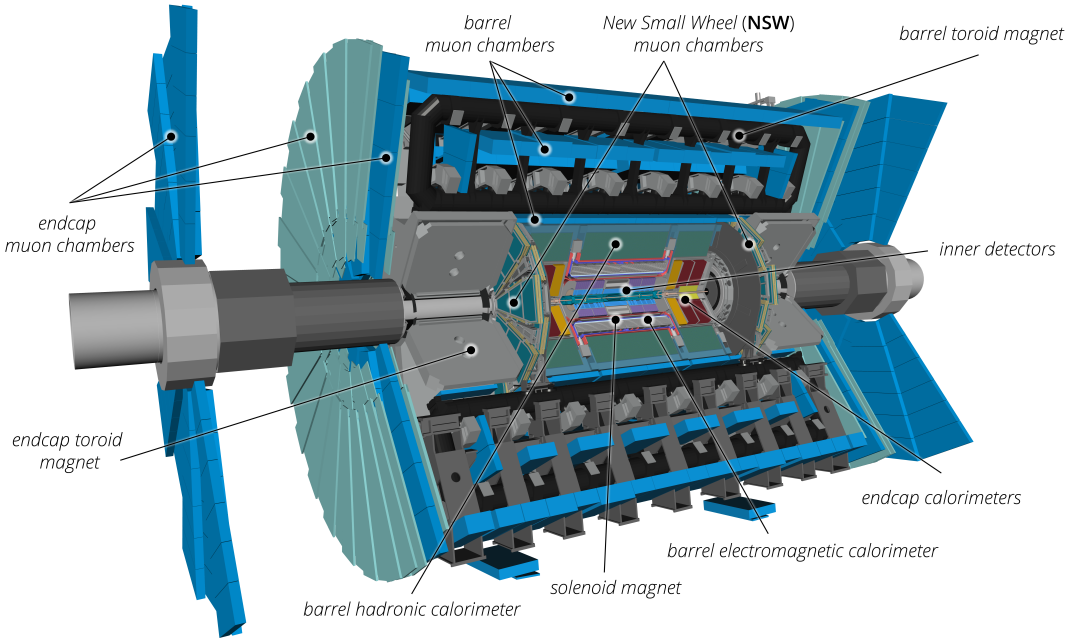

Figure 3.2.: A schematic of the ATLAS detector system with all important subsystems. [11]

of the longitudinal coverage angle and is defined as

$$\eta = -\ln\left(\tan\frac{\theta}{2}\right) \tag{3.1}$$

with θ being the polar angle along the beam pipe. These pixels have a size of 50 $\times$ 400 μm [11] and for the innermost layer 50 $\times$ 250 μm [11], because this close to the interaction point the highest granularity is needed in order to get the best resolution of the ongoing processes. In order to cover the above mentioned region of the detector, around 90 million pixels are needed which makes up 90 percent of the total readout channels of the ATLAS detector.

Surrounding the pixel system is the SCT which is made up of four layers of double-faced microstrips. These around 4000 strips of silicon are combined as pairs at a stereo angle of 2.3° for allowing a 2D measurement and minimising ghost hits that occur if strips are read out simultaneously with more than one combination of possible positions. The strip pitch is 80 μm, and the set has a total of about six million readout channels [11].

The TRT forms the last layer of the ID and is by far the largest in size. While everything up to the SCT takes up a radius of 55 cm the TRT extends the size of the ID to 108 cm

in radius. The η coverage of the TRT only converges to $|\eta| < 2.0$. It is made up of 4 mm thin, 1.4 m long gas drift tubes that consist of a gold plated tungsten wire surrounded by xenon gas. There are 50 thousand of these drift tubes running parallel to the beam pipe and around 250 thousand in the end caps of the detector. A particle penetrating the TRT ideally gives signal in ten of these drift tubes. Additionally to the hits in the drift tubes they provide classification of the particles via transition radiation. However, due to gas leaks and replacement with cheaper Argon gas this transition radiation effect cannot be fully utilised anymore [11]. The momentum resolution of the complete ID system is about $\frac{\sigma_{p_T}}{p_T} = 0.05\% \cdot p_T \oplus 1\%[GeV]$.

Outside of the ID detector sits a solenoid magnet that provides a near homogeneous magnetic field of 2 T for the ID [11]. This magnetic field is used to deflect the charged particles through the Lorentz-force, to better characterize them in the track reconstruction.

Besides the ID, there are other important components of the ATLAS detector. Surrounding the TRT are two layers of calorimeters, the Electromagnetic Calorimeters (ECAL) and the Hadronic Calorimeters (HCAL) with a total pseudorapidity coverage of up to $|\eta| < 4.9$. The ECAL is made up out of passive metal layers of tungsten, copper and lead with active layers of liquid argon in between. When electromagnetically interacting particles enter the ECAL, they deposit a lot of their energy in form of an electromagnetic shower. This can be read out and used as a precise measure for the energy of the particle. The same concept applies to the HCAL where quarks and hadrons shower hadronically. The HCAL is made up out of alternating layers of passive steel and active plastic scintillating tiles which send out photons that are converted to a readout proportional to the energy of the incoming particle. The energy resolution of the ECAL is about $\frac{\sigma_E}{E} = 10\% \cdot \frac{1}{\sqrt{E}}[GeV]$ and about $\frac{\sigma_E}{E} = 40\% \cdot \frac{1}{\sqrt{E}}[GeV]$ for the HCAL [11].

Surrounding the calorimeter layer is the large toroid magnet that supplies the experiment with a magnetic field of up to 3.5 T [11] in order to bend the tracks of charged particles. The outermost layer of ATLAS is formed by the muon chambers at both ends which are used for tracking highly penetrating muons as accurately as possible. With a momentum resolution of $\frac{\sigma_{p_T}}{p_T} = 10\%$ at transverse momenta of $p_T = 1$ TeV the muon chambers cover a pseudorapidity of up to $|\eta| < 2.7$.

3.3. Upgrades and the Inner Tracker

With the High Luminosity Large Hadron Collider (HL-LHC) [13] upgrade on the horizon the ATLAS detector is going to be upgraded as well. One main reason for this is the radiation hardening of the detector components with new technologies because of the increase in luminosity by a factor of 4. This converts to four times more data which needs to be detected and analyzed in time in order to make use of the actual upgrade that is HL-LHC. The upgrade is expected to be finished and running in 2030 as shown in Fig. 3.3 and the ATLAS collaboration has numerous upgrades planned both for software and hardware.

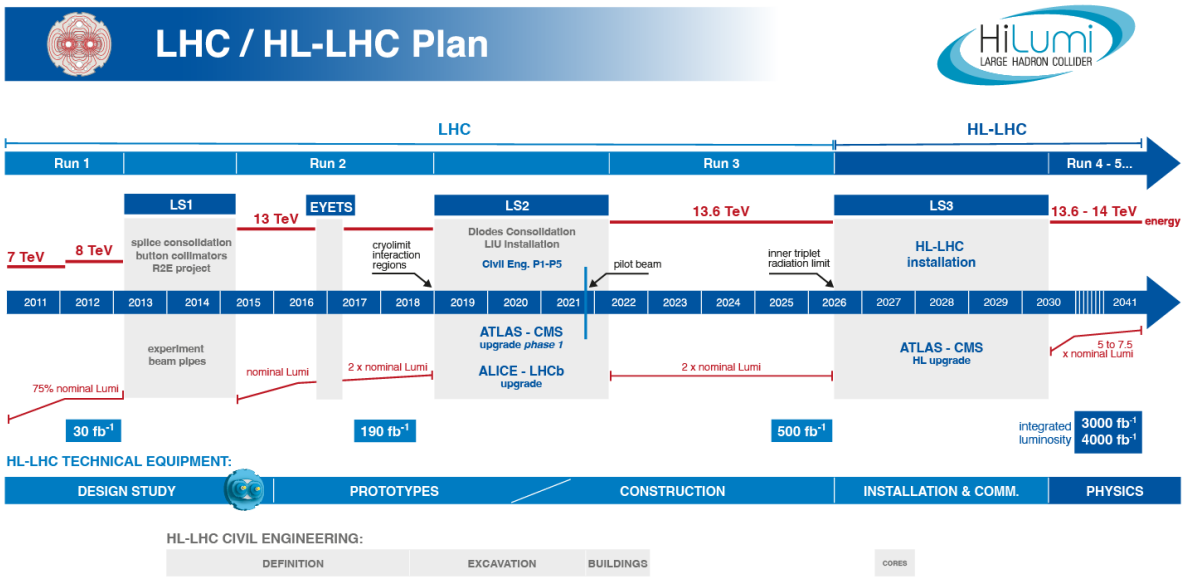

Figure 3.3.: The timetable for the developments at the LHC and HL-LHC [27].

The Inner Tracker (ITk) [12] serves as the upgrade to the current Inner Detector. It is an all silicon based tracking detector that has five layers of pixels in the inner barrel part and four layers of strips in the outer barrel part. The pixel sensors measure 50 μm $\times$ 50 μm with the specialized 3D pixels in the inner layer measuring 25 μm $\times$ 100 μm. Both of the pixel sensor types are made up out of an active silicon layer that is bump bonded to an electronic readout chip. Four of these sensors are grouped together into a module and 14 modules are grouped into a serial powering chain. This enables the implementation of individual bias voltages to counteract radiation damage, as well as reduced material

usage. Strip sensors are made up out of n-type silicon implanted into p-type silicon read out by an electronic chipset every 16 to 60 mm depending on the position in the detector. The pixel as well as the strip sensors are used in the design of the endcaps as well, with multiple layers of pixel sensors and six layers of strip sensors in each end cap, that cover a pseudorapidity of up to $|\eta| = 4$ together with the barrel systems. In total the ITk detector will have over five billion readout channels for the pixels and about 60 million for the strips. The layout of the ITk is shown in Fig. 3.4 and sketch of the dimensions of the ITk with the corresponding pseudorapidity is shown in Fig. 3.5.

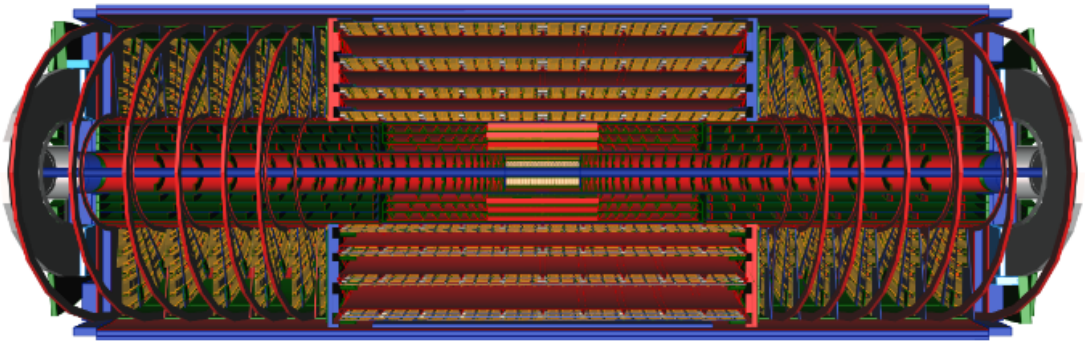

Figure 3.4.: Schematic of the ITk. The Inner Tracker (ITk) layout consists of five layers of pixels in the inner barrel and four layers of strips in the outer barrel as well as multiple angled pixel layers and six strip layers in each endcap[28].

This detector is supported by a specialized subsystem for the forwards and backwards direction which is called the High Granularity Timing Detector (HGTD). The HGTD serves the important purpose of providing time resolution of about 30 ps/track in order to disentangle tracks of charged particles and mitigate pileup. Additionally this addition serves as a measuring device of the luminosity inside the detector. The detector design is comprised of two double-sided layers of silicon sensors of size 1.3 mm $\times$ 1.3 mm that make up the high granularity of the sub detector. Coverage of the HGTD spans the pseudorapidity range of $2.4 < |\eta| < 4$. This totals to 3.6 million readout channels that supply additional information to the track reconstruction. The HGTD is placed in the endcap areas of the detector as shown in Fig.3.6.

Other important upgrades to the ATLAS experiment include improved electronic circuits and power supplies that are sufficiently radiation hard for the calorimeters. Upgrades to the circuits and power supplies are also implemented for the muon spectrometer, together

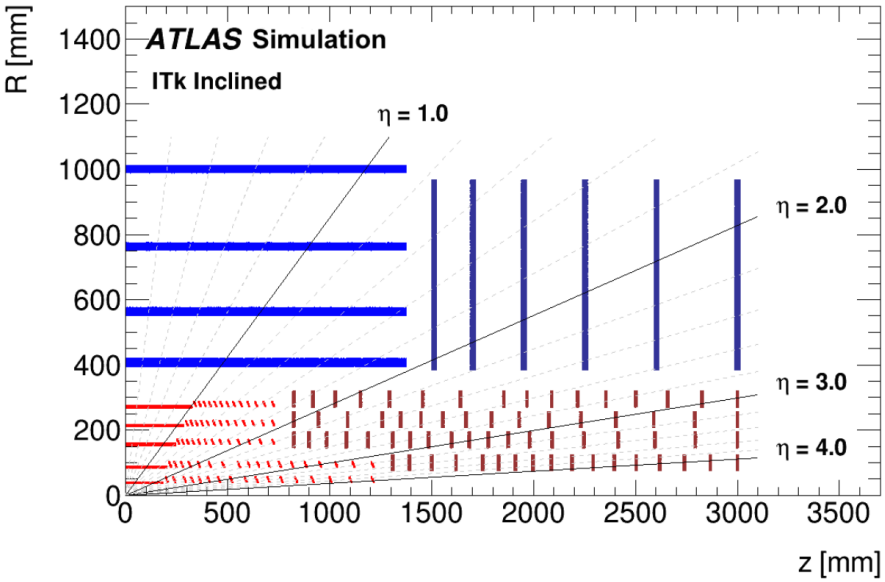

Figure 3.5.: Quadrant of the ITk layout. The Inner Tracker (ITk) covers a pseudorapidity $|\eta|$ of up to 4. Shown in red is the inner system comprised of pixel sensors that are angled towards the interaction point for optimal coverage. The blue parts are the strip sensors that cover much more area as they are further away from the beam pipe, but are less granular than the pixels [12].

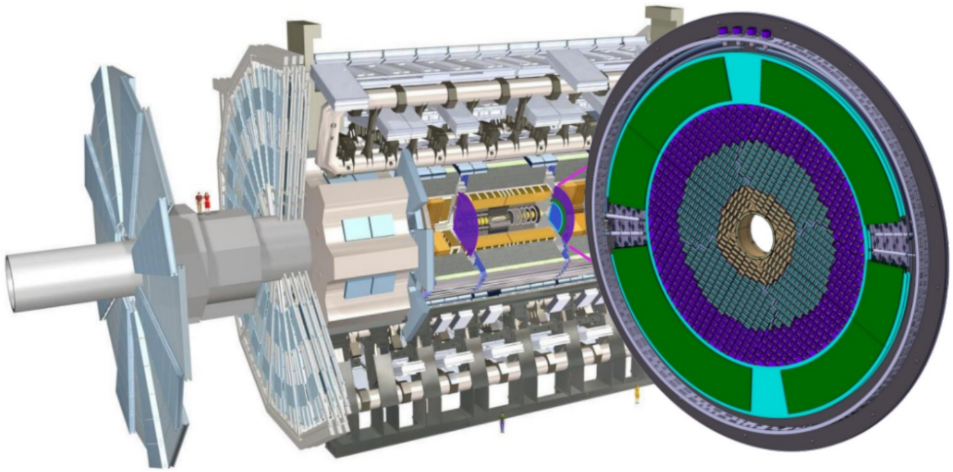

Figure 3.6.: A diagram showing the HGTD in the endcap area of the ITk detector inside the ATLAS detector that provides timing information for track reconstruction to mitigate pileup in the forwards and backwards direction[29].

with the addition of new muon chambers in the barrel region as well as for the inner endcaps. This step should increase the efficiency of muon detection. Upgrades in the

data preprocessing include new improved triggers as well as an improved data analysis setup which need to be ready to process the increased data amounts.

A major issue in the design of a detector located directly outside of the interaction point of the experiment is radiation hardness. This is the reason why the innermost layer of the pixels in the ITk detector is comprised of special 3D pixels that are more radiation hard due to the ionized electron path being shorter because the electrodes are embedded into the sensor itself. The 3D pixels however are much harder to build and therefore much more expensive, which explains their limited use. Also the innermost two layers are designed to be replaceable with a replacement expected after around 2000 fb^{-1} of data collected [12].

Another effort that increases radiation hardness of the ITk detector is its operation in a low temperature environment. The working temperature of -35 degrees Celsius is achieved through a sophisticated carbon dioxide cooling system that needs space in the detector. Similar to the cooling system, there will also need to be made space for cables for data collection and diagnostics, as well as detector control. All of these are integrated in the detector and lead out to both ends of the detector in a region called the Crack Barrel Region which is the focus of this thesis.

The Crack Barrel Region

The Crack Barrel Region (CBR) is the detector region where all of the cables and cooling pipes for ITk enter and exit the Inner Tracker. It is located directly on the inside of the HGTD (Fig. 3.6) at a distance of $\pm$ 3500 mm in the z-direction on both sides of the detector and comprises of structural components and the already mentioned services. All the cables and pipes as well as electronics need to be secured in place for the detector to be organized and well build structurally. Therefore all of these components are mounted on the sealplate, which is by far the largest component of the CBR and is shown in Fig. 3.7 in translucent green as the outer disc. The sealplate is hollow and houses all the cables and pipes as well as two types of devices between two aluminium sheets.

The optoboxes are the first type of device present in the CBR and they serve as signal converters from electrical signals on the inside of ITk for improved radiation hardness to optical signals on the outside for the fastest possible transfer rates. These are shown in Fig. 3.7 in red and are not symmetrically positioned because of asymmetries in the cable routing.

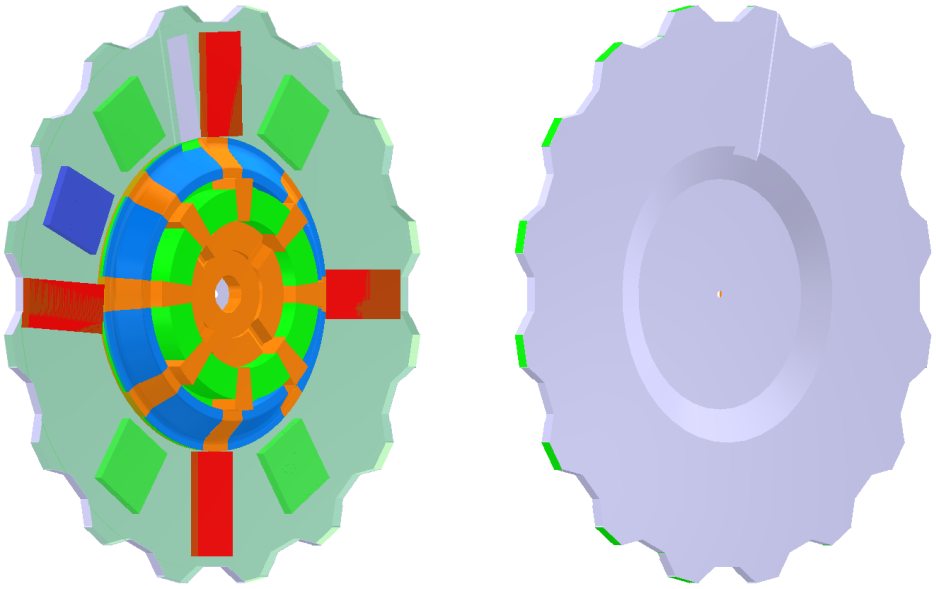

Figure 3.7.: The Crack Barrel Region on the A and C side is shown. It is comprised of four optoboxes in red, five splitterboxes in green and blue, the sealplate in translucent green on the outside and the bulkhead in orange, blue and green on the inside.

While the optoboxes are part of the signal chain, the splitterboxes are used for the distribution of cooling liquids for both the pixel and strip detectors. These are shown in Fig. 3.7 in green and are symmetrical in a group of four, which belong to the strip detector cooling system. The last splitterbox that is shown in blue is used to distribute cooling pipes for the pixel detector.

The bulkhead lies inside the inner opening of the sealplate, where the cables and pipes enter the ITk, and serves as the interface region that contains connectors for all inside and outside service routing and the needed support structures to keep everything in place. The bulkhead region is the most complex part of the crack barrel region because of the engineering challenge of fitting many services in a tight space. It is also challenging from a modelling point of view, as it combines the services of all the different subdetectors. The bulkhead region is shown in Fig. 3.7 in orange, green and blue at the centre of the sealplate.

4. Modelling of the Crack Barrel Region

Modelling of all of the components of the CBR is the main work of this thesis. The basis for the created models are two CAD-model named the ITk Envelope Model (IEM) as shown in Fig. 4.1 and in Fig. A.2, A.3 and A.4 in the appendix and the ITk Services Model (ISM) as shown in Fig. 4.2 and in Fig. A.5 in the appendix. The IEM serves the purpose of defining encompassing volumes for every subpart of the detector without detailing the single cables or structures. On the other hand the ISM is used as a reference for building the detector which means that all details necessary have to be included. Another important differentiation is that the IEM is older than the ISM, so in case of disagreement on some parameters, the ISM has precedence.

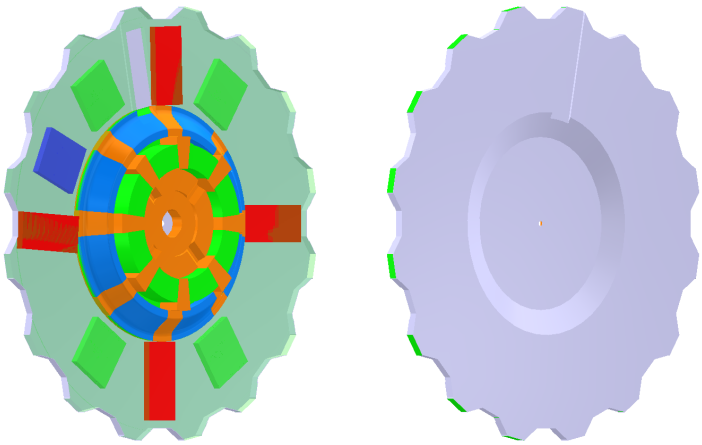

Figure 4.1.: The IEM shown on an angle to better visualize the front and back view as well as the protrusions into the ITk barrel. The left side sealplate is made transparent in order to show the splitterboxes and optoboxes which are hidden inside. The splitterboxes for the strip detector are shown in green and the splitterbox for the pixel detector is shown in blue to differentiate. On the back side shown on the right on can observe the rounded edges and the slope inwards which mimic cables and pipes running there as tightly as possible.

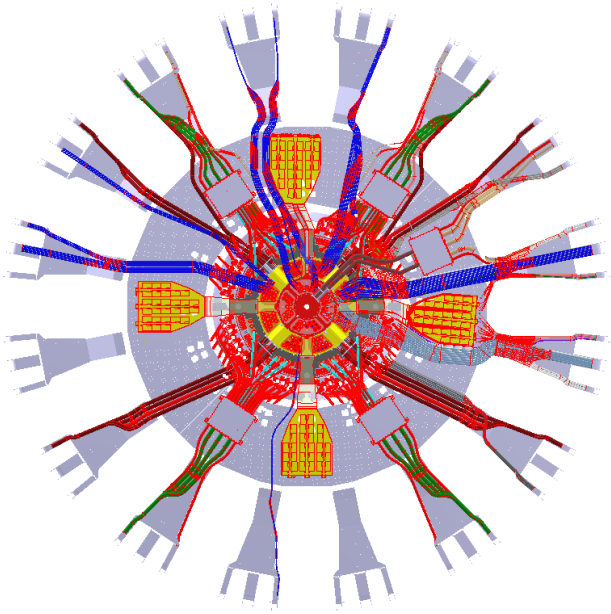

Figure 4.2.: The ISM seen from inside the ITk barrel. This model shows differently shaped optoboxes in yellow and splitterboxes in gray with a red outline compared to the IEM. Also the sealplates' inner radius differs slightly which corresponds to a smaller bulkhead section in the middle that is made up of a lot of cables and pipes. Additionally to the CBR further cables and connectors are shown on the outside, past the outer radius of the sealplate. This model includes all technical detail needed to build the detector and is too complex to be used in simulation, but useful to get crucial information about the geometry.

4.1. Splitterboxes

Splitterboxes are an important part for the cooling systems for both the pixel and the strip detector. They serve as a distribution system for the cooling pipes from larger outside pipes to smaller more numerous pipes on the inside of the detector. Four of the splitterboxes that are positioned symmetrical at angles of 67.5° and 112.5° to each other are used for the cooling pipes of the strip systems. The fifth splitterbox which is positioned at an angle of 32.25° in the larger gap between two boxes serves the same purpose for the pixel systems. The positions in the model are shown in Fig. 4.3.

When comparing the two variants of CAD model (IEM and ISM) for the splitterboxes, the positions are consistent but the dimensions are different. The technical drawings can be found in the appendix in Fig.A.6 and Fig A.10. The technical drawings are mirror images of each other because they were done from opposite sides of the models respectively.

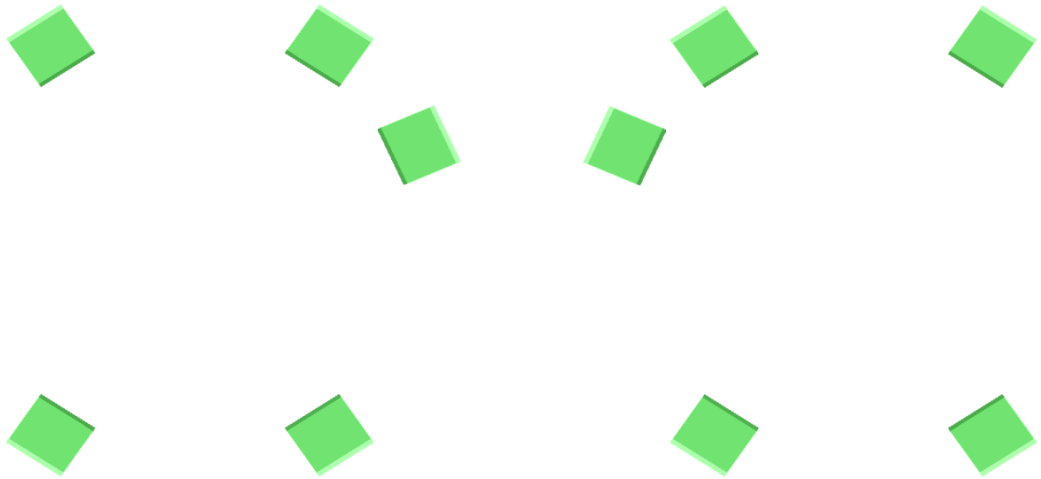

Figure 4.3.: The model of the splitterboxes contains four symmetric boxes and one additional asymmetric box. This asymmetric box is positioned at an angle of 32.25° to the nearest box. The left Fig. shows the A side and the right Fig. shows the C side of the splitterboxes in the GeoModelXML based model as viewed from the outside of the ITk.

For the dimensions of the splitterboxes, the information out of the ISM is used because it is considered more recent. All of the splitterboxes have the same shape and therefore a single splitterbox is defined with the given dimensions of 446.00 mm × 542.13 mm with a thickness of 95.0 mm. This splitterbox is then copied to the five angles of $[24.0°, 56.25°, 123.75°, 236.25°, 303.75°]$ with a radius of $R_{sb} = 1704.84$ mm measured from the inner side of the box. Since the setup for the splitterboxes is mirrored for the A and C side it can be copied for both, and moved to the correct z-position of ± 3405.0 mm. The final result of the model for the A and C side is shown in Fig. 4.3.

4.2. Optoboxes

The optoboxes are an essential part of the detector readout system as they provide a casing for the 224 individual optoboards per optobox which are signal converters that convert electrical signals to optical signals. Electrical signals are used on the inside of the ITk detector because they are more radiation resistant. On the outside of the ITk detector at a z-distance of over 3.5 m from the interaction point, where radiation is not a significant problem for the signal anymore, optical signals are used to maximize the transfer rates for the fastest readout possible. All of the optoboxes are equipped with a cooling system to dissipate the heat produced from the optoboards, and the optoboxes also serve the purpose of organizing the optical setup of the ITk.

For the optoboxes, the CAD-model choice is not as simple as for the splitterboxes. This is because the optoboxes in the IEM as shown in Fig. 4.4 have completely different dimensions and shapes compared to the ISM as shown in Fig. 4.5. As stated previously, the ISM version is the newer and more detailed version and therefore the one chosen for the final model. While the angles with regards to the z-axis are consistent in both models, the rotation of individual boxes on their final positions and the radius of the box positions are not. Together with the differing size of the boxes, this poses the problem of potential overlap with the bulkhead and the sealplate volumes that are modelled after the IEM, as will be explained in Sec. 4.5.

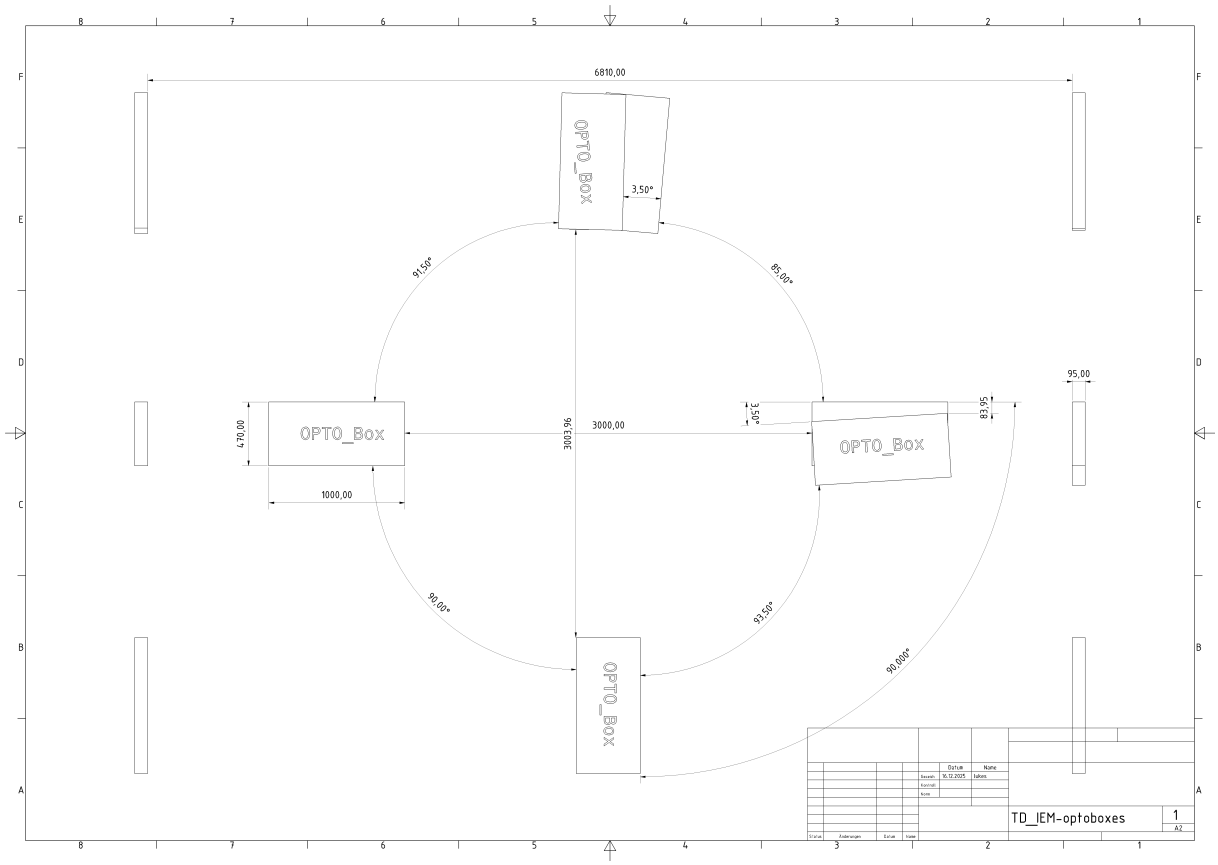

Figure 4.4.: Technical drawing of the optoboxes on the A (front) and C (back) side, created from the ITk Envelope Model. The full sized drawing can be seen in A.7.

Based on these considerations, the optoboxes are implemented similarly to the splitterboxes. First a singular optobox is defined with the dimensions and shape given in the

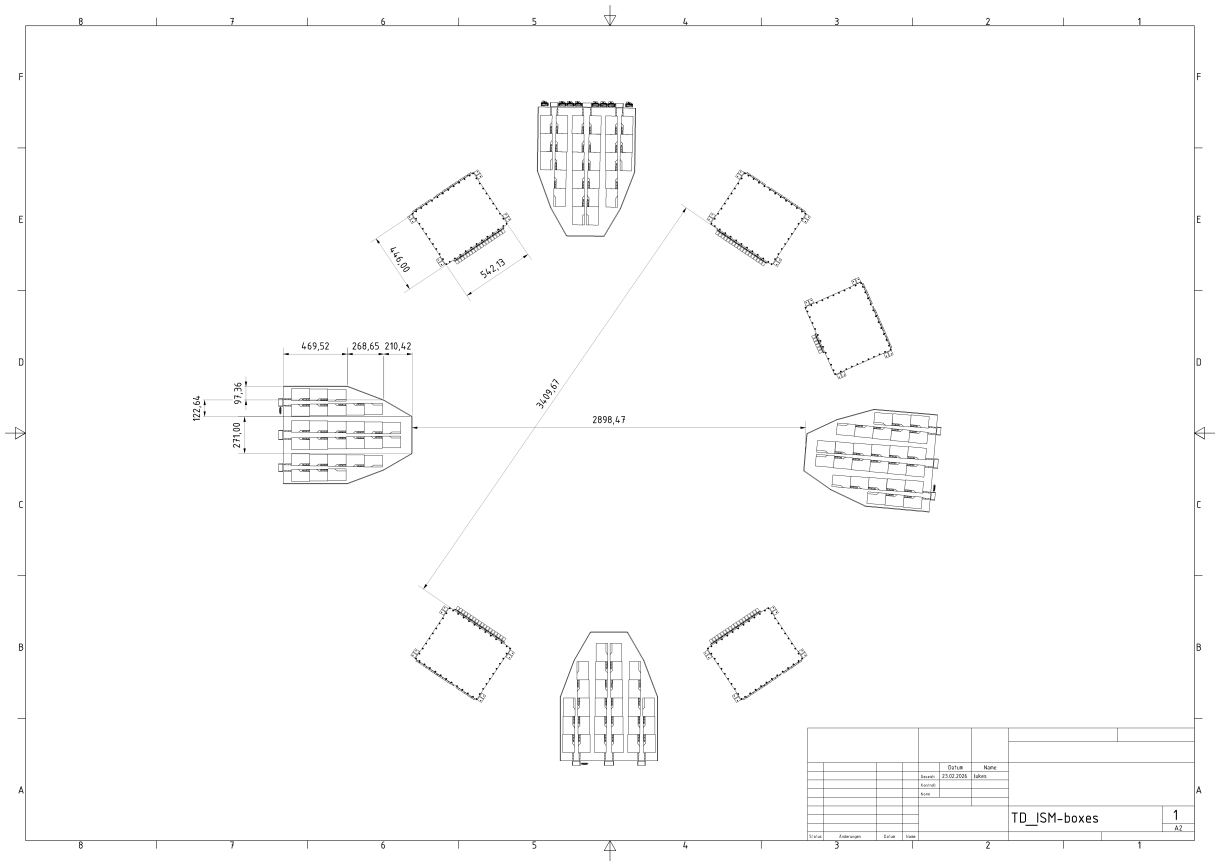

Figure 4.5.: Technical drawing of the optoboxes and splitterboxes on the A side, created from the ITk Services Model. The full sized drawing can be seen in A.10.

ISM as shown in Fig. 4.5. It is important that the optobox shape needs to be modeled as three different shapes which are then positioned with their borders touching to obtain a more complex shape. This shape then contains the correct dimensions and can be rotated and handled as a singular object. This is done with an assembly of the three shapes, whereas an alternative would have been a union of the shapes. The choice to use an assembly instead of a union stems from the fact that a union is a boolean solid, which should intrinsically be avoided as much as possible because of simulation performance as discussed in Sec. 2.3. The use of an assembly does not guarantee that there will not be overlaps of the three shapes, but these overlaps can be resolved by manual adjustments and testing with gmclash.

The optoboxes are then rotated 90.0° and translated to a radius of 1449.24 mm measured from the innermost part of the box. While the splitterboxes possessed rotational symmetry and symmetry in regards to the radial axis, this does not hold for the optoboxes. The optoboxes are not symmetric with respect to the A and C sides, which requires

individual implementation of both of the sides. The asymmetric angles are extracted out of the technical drawing of the IEM because the dimensions are defined more precisely, whereas for the ISM the alignments are much harder to precisely extract.

For the A side, optoboxes 1 and 2 are already in the correct position after the initial rotation and translation. Optobox 3 is rotated around its centre axis for 3.5° and also is shifted in negative y-direction by 81.362 mm. This distance differs slightly from the 83.951 mm seen in the technical drawing of the optoboxes in Fig. 4.4 because of the shift of the edge that the distance is measured to induced by the rotation of the optobox. Optobox 4 is rotated by 1.5° and translated in negative x-direction by 126.142 mm, with the same reasoning as for optobox 3. The final model for the A side of the optoboxes is shown in Fig. 4.6

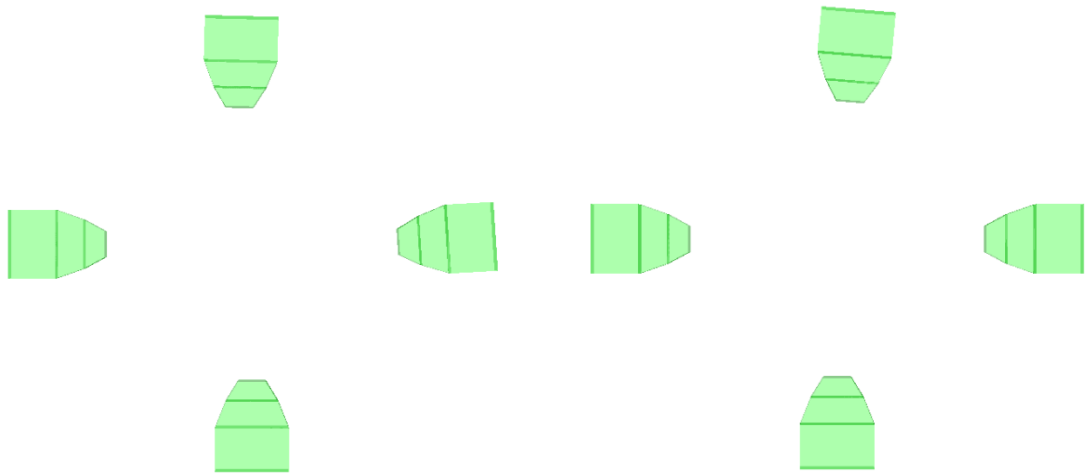

Figure 4.6.: The models of the optoboxes on the A (left) and C (right) side contain the left and lower box on 90 degree angles and the upper and right box slightly shifted from their symmetrical positions.

The C side optoboxes are placed more symmetrically than the A side optoboxes, as optobox 1, 2 and 3 are already in position after the initial positioning, while optobox 4 just is rotated by $-5.0°$ to accommodate the offset shown in the technical drawing in Fig. 4.4. The model of the C side is shown in Fig. 4.6.

The A and C side optoboxes are then shifted along the z-axis to their correct positions at $\pm$ 3405.0 mm respectively which is the same z-coordinate as the splitterboxes.

4.3. Sealplate

Defining the visuals of the Crack Barrel Region more than any other part is the sealplate, spanning 5560.0 mm in diameter and with a thickness of 110.0 mm. The sealplate is the main structural component of the CBR that serves the purpose of containing the cables and cooling pipes from the centre of the detector to the outside. Another main design feature is the mounting of the optoboxes and splitterboxes on the inside of the hollow sealplate to contain all parts of the ITk services in as tight of a volume as possible. The asymmetric part of the sealplate which serves as a channel for cables is also visually notable and is included into the model as well. It is included in the model because the material composition can be updated to differ for the sealplate and this asymmetric part in the future.

Modelling for the Bulkhead is based on the IEM as shown in Fig. 4.7, as it gives a sufficiently detailed description of the geometry. The individual cables and pipes are not needed for this step, as they are described in the ISM as shown in Fig. A.5. While the outer radius and the angular texture are consistent with the ISM, the inner radius for the transition into the bulkhead and services volume is not consistent between the two CAD models. The inner radius of the sealplate and the outer radius of the bulkhead are therefore adjusted to the value provided in the ISM, as it is the newer model.

The basis for the model is a hollow tube of thickness 110.0 mm with an outer radius of 2600.0 mm and an inner radius of 1425.0 mm as shown in Fig. 4.8 in red. Following the definition of the tube, the shape of the asymmetric box is implemented with the same thickness as the tube and a length of 1437.62 mm and width of 323.02 mm. The box then is subtracted from the tube to form the space into which the volume of the box fits.

The next step is the definition of a trapezoid that is copied a total of 15 times with an angle of 22.5° in between copies. This trapezoid has a base length of 697.85 mm and a top length of 323.02 mm with its thickness being equal to that of the tube as specified above. For the 16th trapezoid there needs to be a subtraction of the trapezoid with the asymmetric box. It is important to note that the definition of a boolean solid can only be done for shapes. Because copying of volumes can only be performed for the already implemented logvols with assigned materials, the resulting subtraction needs to be defined and moved individually to the location of the 16th trapezoid, which is at the angle of the asymmetric box. The trapezoids can be seen in Fig. 4.8 in red. The final step is the insertion of a logvol with the shape of the asymmetric box into the created slot as shown

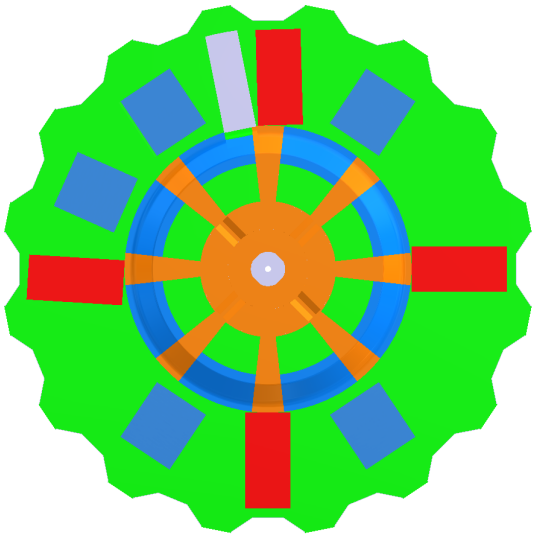

Figure 4.7.: The IEM seen from the inside of the ITk detector. All of the optoboxes in red and splitterboxes in blue sit on top of the sealplate. The outer green volume is the structural sealplate and the housing for cables, pipes and the boxes. The light blue, orange, and inner green part are all subvolumes of the bulkhead which encompasses cables, pipes and connectors. An asymmetry is shown on the top, left of the optobox in red, which is a box that houses cables. A bigger graphic of this is shown in Fig. A.2 and additional ones in Fig. A.3, A.4.

in Fig. 4.8 in yellow.

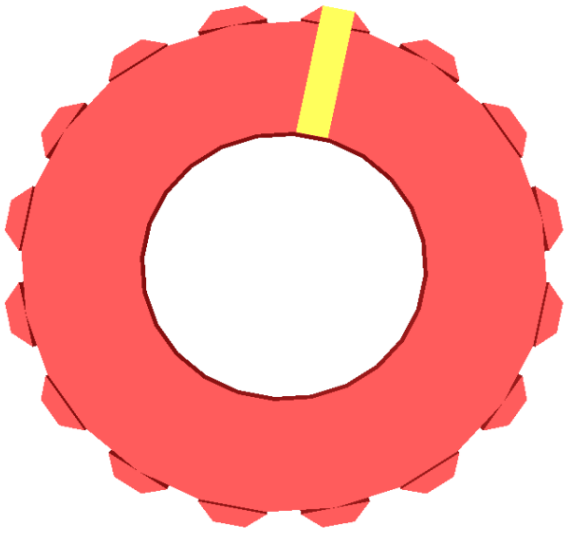

Figure 4.8.: The model of the sealplate shown from the outside of the detector is made up of a hollow tube as well as 16 small trapezoids positioned on the outside of the tube. An asymmetry in form of a rectangular box is placed in a cutout at an angle of $-11.25°$ from the top.

4.4. Bulkhead

The bulkhead serves as the interface of the ITk, as every cable and pipe that enter and exit the ITk detector is connected here. Due to the complexity of the wiring and the number of components involved, this structure is the most complex part of the CBR, both in the physical experiment and in the model that is built for the simulation. Since it is also the part of the model that is closest to the beam pipe, and therefore in the most forward region of the pseudorapidity, it is important to model the bulkhead accurately.

One aspect that adds to the complexity of the implementation is that the cables of the different detector subsystems are tightly fitted together without gaps as shown in Fig. 4.9, and therefore the modelling of the bulkhead is not that straightforward. The solution is to combine the service volumes of the different subsystems that are the pixel services, strip services and strip endcap services into one volume. This is done to minimize volumes and computation time, and also because the reduced complexity does not impact model quality as much because the materials present are similar in all three subsystems.

Another challenge when modelling the bulkhead was deciding how to model all parts that have rounded edges as again shown in Fig. 4.9 on the far right. The solution applied

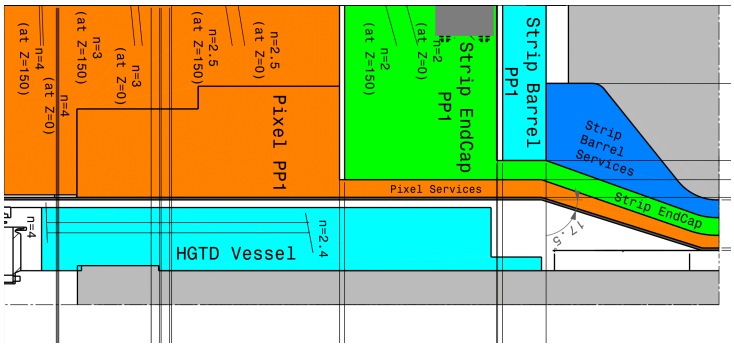

Figure 4.9.: A cross sectional view of the critical area where the services of the pixel (orange), strip (blue), and strip endcap (green) sub detectors are packed tightly together at the right of the image. It has to be noted that the HGTD Vessel and the grey structural parts are not part of the CBR.

for rounded edges is to approximate the round edge with a volume that has two straight edges for simplification. It is important however that the approximated edge is defined inside the original dimensions of the volume because else it can become a problem when protruding into adjacent volumes. Another possible solution that was discarded is the use of boolean solids. While doing a subtraction of a tube with some object with a rounded edge to obtain a more detailed model would be closer to the real physical dimensions, the use of boolean solids and decreased performance is not justified for a diminishing increase in accuracy.

Based on these simplifications, the IEM was the more suitable choice as a basis for the GeoModelXML based model because it already includes the merging of the individual service volumes into one volume. The technical drawing is shown in Fig. 4.10.

Starting from the outside, the model is made up out of two cone sections. The first cone section has an outer radius of 1425.0 mm for both faces and extends into the centre to the radii of 1343.068 mm and 1034.0 mm respectively, to form an inverse cone that has its slope pointing inwards to the beam pipe. For the second cone section, the slope points outwards with the inner two radii being equal and measuring 1034.0 mm, whereas the slope is defined by the outer radii of 1343.068 mm and 1126.0 mm. The cone sections are best visualised in a side view as shown in Fig. 4.12

Continuing inwards, the next challenging part is the modelling of the two different cross sections that define the inner part of the model. This is done with tube sections which sit

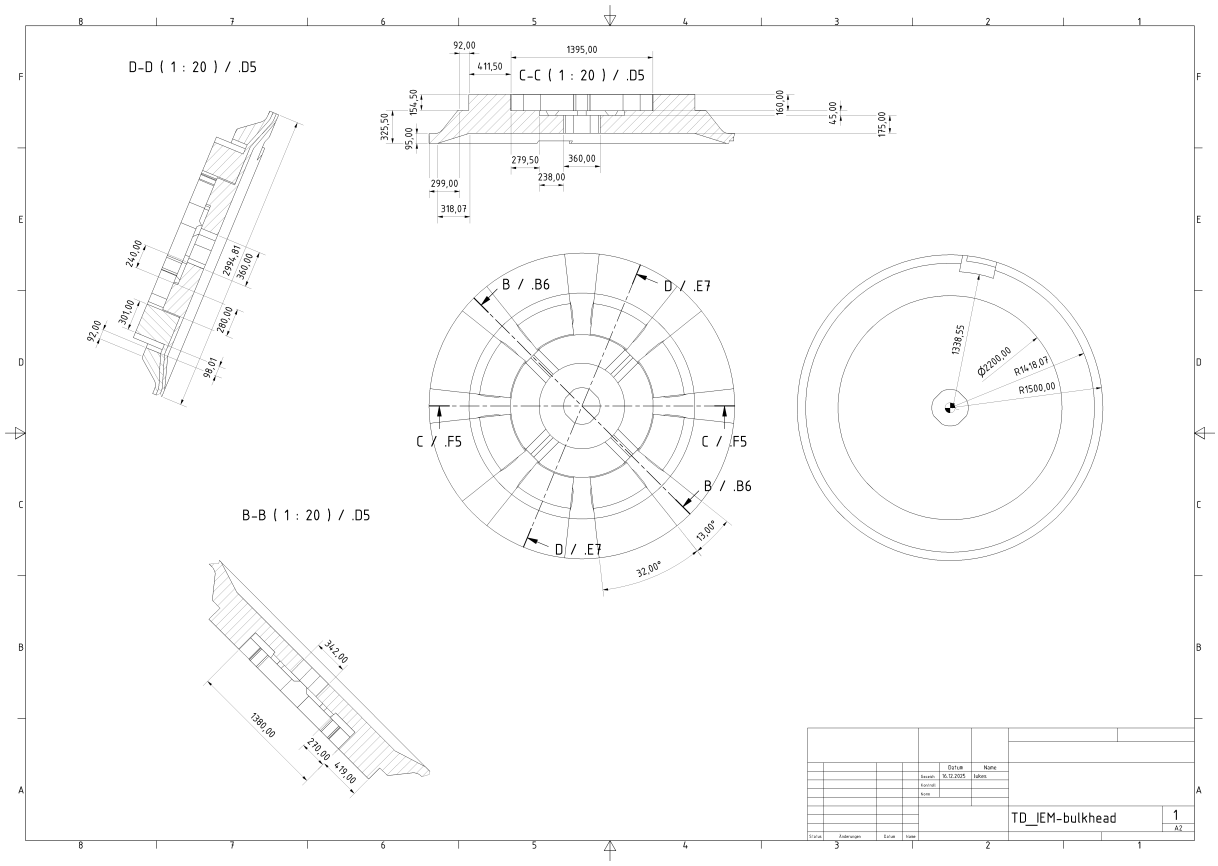

Figure 4.10.: Technical drawing of the bulkhead, created from the ITk Envelope Model. The full sized drawing can be seen in Fig. A.9.

tightly together without any gaps in between. The biggest tube sections are placed spanning the radii from 622.5 mm to 1034.0 mm and an angle of 32.0° each. There are eight of these tube sections in total and they are placed symmetrically with 45.0° between them. The positioning along the z axis on the outside is flush with the neighboring cone section, but also protrudes to the inside of the detector at a total length of 380 mm, which is 160.0 mm longer than the cone section. For the second tube section, the length and inner radius is the same, but the outer radius is only 923.5 mm, which leaves a gap. This gap is filled with tube section three which spans from 923.5 mm to 1034.0 mm, but only has a length of 60.0 mm and therefore does not protrude further than the cone section in the direction of the origin. A cross sectional view that highlights the profile is shown in Fig.4.12.

The last missing volume is covered by one tube section spanning the radii of 622.5 mm and 343.0 mm, with a length of 220.0 mm, and another tube that is defined through the radii of 343.0 mm and 105.0 mm with a slightly shorter length of 175.0 mm. These two tube sections sit flush with the aforementioned tube sections on the outside away from

the origin. The finished model is shown in Fig. 4.11 and Fig. 4.12.

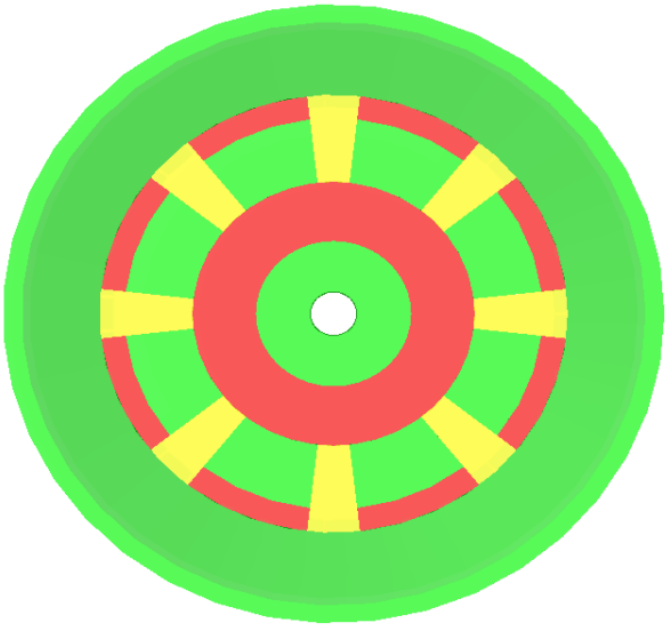

Figure 4.11.: The model of the bulkhead is made up out of the two outer cone sections in green and the three different types of tube sections in yellow, green and red. The middle part contains two hollow tubes in red and green with slightly different thickness. The back view shows the symmetry as well as the plane back part of the model with the outer cone section sloping inwards.

Figure 4.12.: The cross section of the bulkhead model shows two different cross sections depending on the angle of the cut. On the left on can observe the cross section with the two tube sections of differing height in green and red and on the right the singular tube section in yellow. Also the two cone sections can be seen in green on the outside.

To conclude, the model for the bulkhead is translated in the z-direction to its z-position of $\pm$ 3500.0 mm at the point furthest from the origin in z-direction which is the top part of the inverse cone section.

4.5. Merging of the Different Geometries

It is very practical to split the GeoModelXML model creation for the CBR into different parts for easier construction. The problem that comes with this however, is that in the end all of the parts need to be merged together to create a final model that has the right dimensions without any overlap or protrusions of volumes. This is especially a problem when working with two different base models in the IEM and the ISM.

The main difference between these two models is the radius where the bulkhead ends and the sealplate begins, which is about 75.0 mm larger in the IEM. The optoboxes which are modelled after the ISM protruded into the bulkhead which was modelled based on the IEM as a result of using two different models as a basis for one implementation of another model. The solution that was applied was a rescaling of the bulkhead to the described outer radius in the ISM, because the geometry does not have any notable differences, and the model is only an approximation. Since the innermost radius did not change, as the beam pipe still needs to fit there, the rescaling is absorbed in the innermost tube by making it span 75.0 mm less in the radial direction. The fully assembled model of the CBR is shown in Fig. 4.13 from a frontal view and Fig. 4.14 from an angle.

After this rescaling of the bulkhead, the assembly of the model from the submodels is implemented with several checks. First, a visual check is performed to see if any parts need to be rotated because they are not aligned correctly. This is followed by a code review with focus on all of the used angles of rotation. The second check consists of correctly aligning all of the components on the z-axis, where both a visual and code review confirm that volumes that should be flush actually are flush and do not exhibit protrusions. After an alignment in the z-direction, the radial alignment is done where all of the radii are checked in the code, and a visual check confirms that there are no visual protrusions or gaps between adjacent volumes in the radial direction. A clash check with gmclash finalizes the review of the finished model. As seen in Fig. 4.15 there were numerous clashes which were resolved by making geometrical corrections of order 0.1 mm.

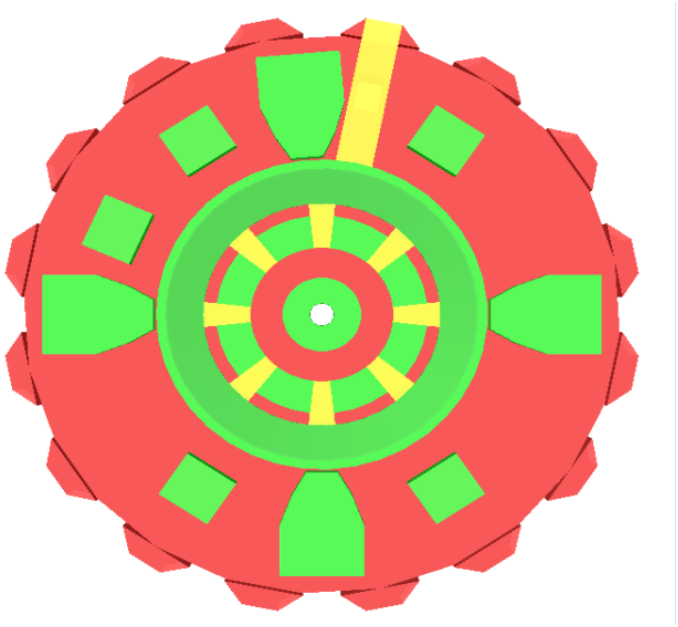

Figure 4.13.: The completed model of the C side with the sub components of four optoboxes in green, five rectangular splitterboxes in green, the sealplate in red with a yellow asymmetry on the outside and the bulkhead on the inside. This view is from the outside of the ITk detector.

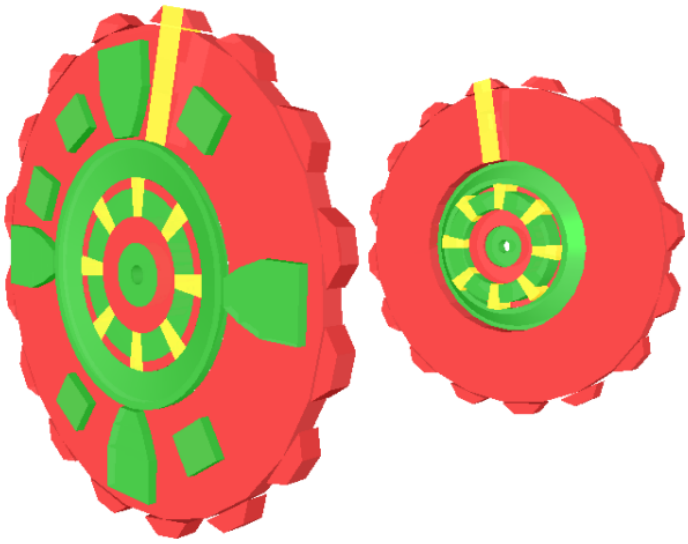

Figure 4.14.: The finished model with the correct alignment of both the A and the C side on the z-axis. The dimensions of the real detector counterpart are about six meters in diameter and eight meters across.

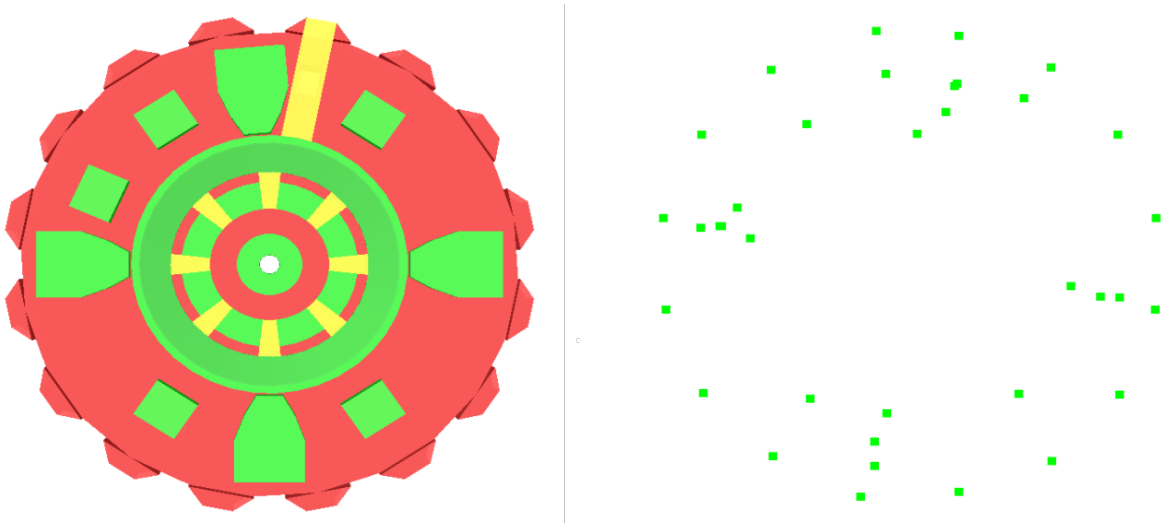

Figure 4.15.: The visualisation of the first results of gmclash (right) used on the merged GeoModelXML based model (left). The clashes shown can be identified with all of the subvolumes of the boxes and the outer trapezoids clashing with the sealplate and the asymmetric box clashing with the sealplate and the outer trapezoid.

4.6. Material Definitions

Without the implementation of accurate materials, the definition of the correct geometry is not useful for an accurate physics simulation. The correct density of material inside the detector model is of great importance because this affects the tracking performance and plays a great role for the material budget. The material implementation is done in close exchange with engineers of the ITk, because specifying the correct materials to fill the volumes can be difficult, and the CAD models do not specify the materials used to the extent needed in the GeoModelXML model. Furthermore the materials need to be defined with respect to the geometry implementation. It is important to define the overall mass in the model to be as close to the real mass of the corresponding real components, in order for mass integration over the model to yield similar results to the mass of the experiment.

The material definitions in the GeoModelXML based model are currently only completed for the optoboxes. The reason for unfinished material definitions of the splitterboxes, sealplate and bulkhead is because the information of the exact materials is not yet fully available. This problem will be discussed further in Chapter 6.

For the optobox system, numerous materials are combined to implement an accurate

density and material blend that represents the real physical materials as close as possible. A singular optobox is made up out of an aluminium casing, the cooling system of steel pipes and the 28 stacks of 8 optoboards.

The parameters needed for the material implementation of volumes in GeoModelXML are the overall density as well as the percentages of the materials contributing to that density. This means that the total volume and mass of the different components of the optoboxes need to be converted into the density they contribute to the geometry. The formula used to acquire the density of a given volume V is

$$\rho = \frac{m}{V} \tag{4.1}$$

where m is the mass of the material in the volume. In order to calculate the proportions of the materials in the total optobox volume, the mass of the given material is divided by the total mass of the optobox to acquire the contribution percentage.

For the aluminium casing, the material composition is 100% aluminium and the total volume is 10803 cm^3 including the walls, lid and the bottom cooling plate. With the density of aluminium being 2.7 $\frac{g}{cm^3}$, this results in a mass of 29.17 kg.

The cooling pipes inside the optobox are made up out of 100% stainless steel with a density of 7.86 $\frac{g}{cm^3}$. The occupied volume of the stainless steel is 65.6 cm^3 and the resulting mass is 0.52 kg.

Since the optoboards are complex electrical components, their material composition can only be estimated. For this reason, a material preset in the existing geometry called ChipPCB is used. This material is comprised of 95.9% Silicon and 4.1% copper which is a good approximation for a circuit board. In total, the mass of the optoboards together with support structure is 20.16 kg, and this mass is modelled with the ChipPCB material. The reason why support structure is not calculated separately is because the information is not available and the effect of it would be negligible.

In order to implement these considerations, the average density of an optobox is defined out of the total calculated mass of 49.85 kg per optobox over the total volume of the GeoModelXML based optobox model which is 56432 cm^3. The resulting density is 0.88 $\frac{g}{cm^3}$, with the percentages of the materials being calculated based on their volumes.

These percentages are 19.14% of aluminium, 14.87% of ChipPCB and 0.12% of stainless steel with the rest of the volume being air. This density might seem low, but this is the result of air contributing to the volume, because there are many gaps between the circuit boards. Additionally the cables included in the optobox are currently not yet included in the calculation, as there is no information available about them currently. Therefore the remaining 65.87% of the total optobox volume is modelled as air until further information on the cables is implemented.

The materials of the other components of the CBR will be implemented in the future, with the same concept that was presented in this section.

5. Model Comparison and Results

5.1. Visual Comparison with the CAD-Model

The visual comparison with the two CAD models is a good measure of accuracy for the new GeoModelXML based CBR model. It has to be noted that the colours do not match and are only for visualisation. A visualisation of the two models is shown in Fig. 5.1.

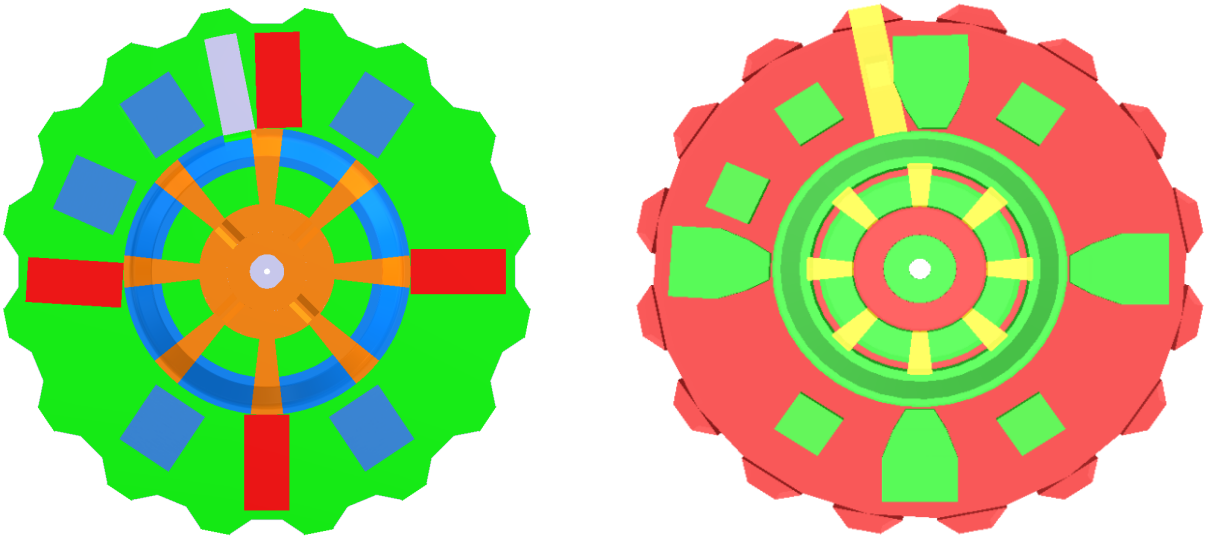

Figure 5.1.: This figure shows the A side of the CBR implemented in the IEM-CAD model on the left and the GeoModelXML model on the right. The view is from the inside of the ITk detector looking outside.

On the outside, the shape of the trapezoids in the GeoModelXML model very closely resembles the spikes on the outside of the IEM. One notable visual difference are the small holes between trapezoid and the tube part of the sealplate, which appear because the tube section has a round edge, whereas the trapezoids possess a flat inward section. The resulting gap is not a big problem for the simulation because it is very small and the likelihood of a particle seeing reduced material interactions because of the gap is very

small. Implementing the sealplates outer protrusions in this way however simplifies the geometry significantly and is therefore a good solution.

Moving inwards, the main section of the sealplate which is coloured in green in the IEM and in red in the GeoModelXML based model has the same outer radius. The inner radius of the GeoModelXML based model however is smaller by 75.0 mm as already mentioned in Section 4.5. This rescaling can be seen in all of the components moving inwards as well, except in the innermost hole which needs to be big enough to fit the beam pipe. The reason why this rescaling is necessary can be observed very well on the optoboxes in red in the IEM and four green bigger optoboxes in the GeoModelXML based model.

For the optoboxes, the shape as well as the positions have changed significantly visually. From the first draft in the IEM, where the optoboxes are modelled as rectangular boxes in red, the shape defined in the ISM model as shown in Fig. 5.2 is the more accurate representation. The ISM implementation is the more up to date and therefore implemented in the GeoModelXML based model in green. This argument also holds for the splitterboxes, for which the shape has been adjusted as well to fit the description in the ISM as shown in Fig. 5.2. In addition to the shape, the radial position of the optoboxes shifted inwards as well in the ISM and together with the slightly longer optoboxes in the ISM this causes the 75.0 mm rescaling. If the inner radius of the sealplate would not have been adjusted, the optoboxes would have protruded into the bulkhead volume which is not physical. Therefore the rescaling of the whole inner bulkhead section is necessary.

The bulkhead is the most complex section visually as well as in the implementation. The visual appearance of the bulkhead is very similar in the IEM and the GeoModelXML based model, despite the aforementioned rescaling that was done for the GeoModelXML based model in Section 4.5. One visual difference is the eight orange protrusions in the IEM which span up to the sealplate, whereas in the GeoModelXML based model they only span to the sloped cone section. This however, is only due to the colouring in the two models being different and is not a difference in the geometry. In the IEM, all of the orange geometry is part of the pixel services, and the blue geometry is part of the strip barrel services. The actual volume in the sloped part is 360° symmetric though, as can be seen in the technical drawing in Fig. A.9 in all of the three cross sections. This requires the services of the different subdetectors to be treated as a singular volume which was part of the implementation of the GeoModelXML based model, as explained in Section 4.

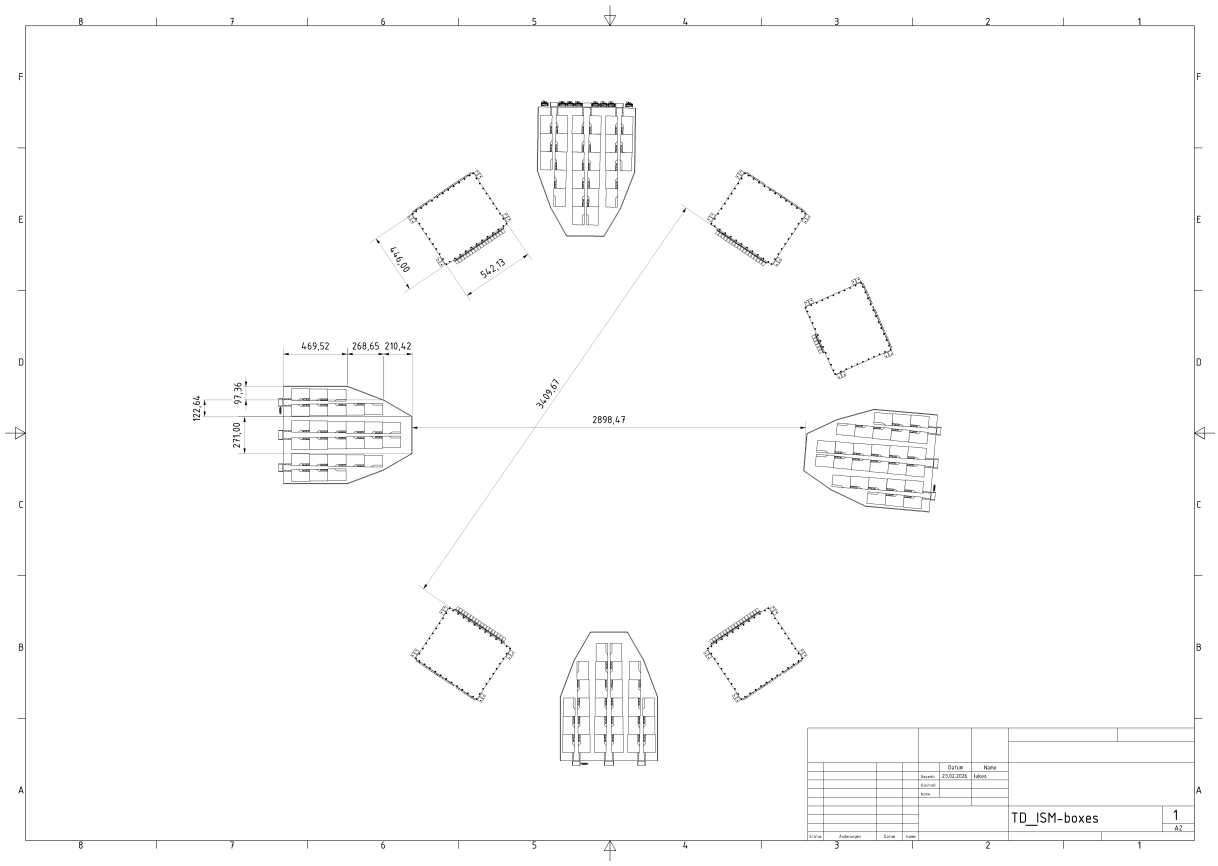

Figure 5.2.: Technical drawing of the optoboxes and splitterboxes on the A side, created from the ITk Services Model. A bigger figure is found in the appendix in Fig. A.10

An additional visual inconsistency is the small sections in between the aforementioned orange sections in the IEM, as shown in Fig. 5.1. These eight sections are made up out of two tube sections with different height and are consistent between the two models, but both coloured green in the IEM and coloured green and red in the GeoModelXML based model. The last visual difference can be found in the second inner ring, where in the IEM, four asymmetries can be found to be separated by 90°. These do not show up in the GeoModelXML based model because they would have made modelling unnecessarily complex. Considering these are only small indentations in the second inner ring, the effort and additional use of boolean solids or multiple geometries is not justified.

The last visually different part between the IEM and the GeoModelXML based implementation is the assembly in the z-direction. The optoboxes and splitterboxes in the IEM are like in the actual physical CBR included inside the sealplate, whereas for the

GeoModelXML based model, they are just adjacent on the outer side of the sealplate. If the boxes would be modelled inside of the sealplate volume, holes of the size of the boxes would need to be cut inside the sealplate volume with multiple subtractions. This is not justified because it would lead to increased simulation times for diminishing returns in accuracy. Because of this, the implementation of the sealplate is done without the use of subtractions for the optoboxes and splitterboxes. An alternative that could be implemented is the use of two thinner sealplates with the optoboxes and splitterboxes in between. This alternative needs to be adjusted to the material implementation in the sealplate and is therefore not to be tested until the material implementation inside the sealplate geometry is completed.

6. Conclusion

In the ongoing pursuit to explore the secrets of nature, the Large Hadron Collider at CERN will be upgraded to the HL-LHC to increase the possibilities for physics analysis. The ATLAS experiment located at CERN is in preparation with both software and hardware upgrades to make use of the new possibilities. For the ITk, the new inner tracking detector of the ATLAS experiment the simulation model still is not completed, with one missing part being the Crack Barrel Region that houses services and supporting structural components. The creation of this model of the ITk services in the Crack Barrel Region is the focus of this thesis.

The ITk Crack Barrel Region geometry has been successfully implemented as a GeoModelXML based model. This includes the different subsystems of the splitterboxes, optoboxes, sealplate and bulkhead. Furthermore the implementation of correct materials for the optoboxes has been implemented as an example for the other subsystems. The geometry is clash free and therefore usable and has been validated by visual comparison with the existing CAD models that it is sufficiently detailed to be an accurate representation of the CBR inside particle physics simulations.

I have familiarized myself with the GeoModelXML toolkit as well as coding with XML. A significant amount of my time was spent learning the different possibilities and restrictions that the toolkit poses and becoming accustomed to the coding conventions already in use from other members of the ATLAS collaboration.

In addition to learning the implementation, the knowledge to interpret CAD files and extract information efficiently was also obtained. This includes visualisation and reading of geometries as well as the creation of technical drawings of the relevant geometry. It is important to note that working with two completely different models and to combine the extracted information was a considerable challenge.

The creative part of the work was especially interesting, including making decisions on

how much technical detail was necessary for the implementation as well as on which parts to simplify for more efficient simulation. When creating the technical drawings, the angle of the visualisation and included details like cables, pipes or connectors often needed to be redone many times over which improved the understanding of the underlying geometry and its visualisation.

The acquired knowledge and abilities in this thesis as well as the finished geometry of the GeoModelXML based model of the CBR show the possibilities for upcoming implementations and further work on the subject of detector description with GeoModelXML for the ATLAS experiment.

In the future, the material definitions of the splitterboxes, sealplate and bulkhead will be implemented. The information is mostly available after much exchange with engineers and additional research. Therefore the implementation of the rest of the GeoModelXML based model of the CBR is mostly a matter of time. In addition to the materials, small improvements to the geometry as mentioned in Section 5.1 could be implemented as well as external feedback.

The next big step is integration into the existing ITkLayouts repository, which is the complete GeoModelXML based model for the ITk detector. This integration process has already been started and first comments on the implementations already have arrived. A geometrical review in terms of overlap tests with gmclash together with the rest of the ITk geometry still needs to be done as well as performance tests. The outdated model of the CBR that my work aims to replace is comprised of only three tubes which give a very rough estimation of the geometry, so the work shown in this thesis will certainly be a big improvement for the GeoModelXML based detector description model.

In the summer of 2026, the LHC will shut down from Run 3 to the upgrading phase for the HL-LHC. During that shutdown, the ATLAS and CMS experiments will upgrade both software and especially hardware components. The preparations for these upgrades are already underway with great anticipation for the start of Run 4 in June 2030. The new accelerator technologies combined with the most powerful particle detectors ever built will push the limits of high energy physics and will aid many interesting discoveries that are to come. For ATLAS, the ITk will be a key component to enable more precise measurements of particle physics processes. One focus for ATLAS lies on the discovery of new physics beyond the SM. Another goal is the experimental observation of Higgs boson

pair production. Measurements of such processes compared with accurate simulations will define important missing parameters of the Standard Model of particle physics and will allow mankind to become one step closer to a more accurate description of nature.

Bibliography

[1] S. L. Glashow, *Partial Symmetries of Weak Interactions*, Nucl. Phys. **22**, 579 (1961)

[2] S. Weinberg, *A Model of Leptons*, Phys. Rev. Lett. **19**, 1264 (1967)

[3] A. Salam, *Weak and Electromagnetic Interactions*, ed. Nobel Symposium No. 8 (Almqvist & Wiksell, Stockholm, 1968)

[4] M. Gell-Mann, *A schematic model of baryons and mesons*, Phys. Rev. Lett. **8(3)**, 214 (1964)

[5] P. Higgs, *Broken symmetries, massless particles and gauge fields*, Phys. Rev. Lett. **12(2)**, 132 (1964)

[6] P. W. Higgs, *Broken Symmetries and the Masses of Gauge Bosons*, Phys. Rev. Lett. **13**, 508 (1964)

[7] H. Fritzsch, M. Gell-Mann, H. Leutwyler, *Advantages of the color octet gluon picture*, Phys. Rev. Lett. **47(4)**, 365 (1973)

[8] T. M. P. Tait, C.-P. Yuan, *Single Top Quark Production as a Window to Physics Beyond the Standard Model*, Phys. Rev. D **63**, 014018 (2001), `hep-ph/0007298`

[9] H. E. Haber, G. L. Kane, *The search for supersymmetry: Probing physics beyond the standard model*, Phys. Rep. **117**, 75 (1985)

[10] L. R. Evans, *The Large Hadron Collider (LHC)*, Eur. Phys. J. C **34**, S11 (2004)

[11] The ATLAS Collaboration, *The ATLAS Experiment at the CERN Large Hadron Collider*, JINST **3(08)**, S08003 (2008)

[12] *Technical Design Report for the ATLAS Inner Tracker Pixel Detector*, Technical report, CERN, Geneva (2017), URL `https://cds.cern.ch/record/2285585`

[13] G. Apollinari, O. Brüning, T. Nakamoto, L. Rossi, *High Luminosity Large Hadron Collider HL-LHC*, CERN Yellow Rep. **(5)**, 1 (2015), `1705.08830`

[14] R. L. Workman et al. (ParticleDataGroup), *Review of Particle Physics, 2022-2023*, Progress of Theoretical and Experimental Physics **2022(8)**, 083C01 (2022)

[15] *Standard Model of Elementary Particles*, `https://en.wikipedia.org/wiki/File:Standard_Model_of_Elementary_Particles.svg` (2019), [Online; retrieved 01.03.2026]

[16] The CKMfitter Group, J. Charles, et al., *CP Violation and the CKM Matrix: Assessing the Impact of the Asymmetric B Factories*, Eur. Phys. J. C **41**, 1 (2005), `hep-ph/0406184`

[17] K. G. Wilson, *Confinement of quarks*, Phys. Rev. D **10**, 2445 (1974)

[18] ATLAS Collaboration, *Observation of a new particle in the search for the Standard Model Higgs boson with the ATLAS detector at the LHC*, Phys. Rev. Lett. **716(1)**, 1 (2012)

[19] M. Thomson, *Modern Particle Physics*, Cambridge University Press (2013)

[20] A. Lechner, *Particle interactions with matter*, CERN Yellow Rep. School Proc. **5**, 47 (2018)

[21] D. Michael et al., *The magnetized steel and scintillator calorimeters of the MINOS experiment*, Nuclear Instruments and Methods in Physics Research Section A: Accelerators, Spectrometers, Detectors and Associated Equipment **596(2)**, 190 (2008), URL `https://www.sciencedirect.com/science/article/pii/S0168900208011613`

[22] S. Agostinelli, et al. (Geant4), *GEANT4: A Simulation Toolkit*, Nucl. Instrum. Meth. A **506**, 250 (2003)

[23] Merkt, Sebastian Andreas, et al., *Going standalone and platform-independent, an example from recent work on the ATLAS Detector Description and interactive data visualization*, EPJ Web Conf. **214**, 02035 (2019), URL `https://doi.org/10.1051/epjconf/201921402035`

[24] *Schematic overview of the CERN accelerator complex*, `https://www.researchgate.net/figure/Schematic-overview-of-the-CERN-accelerator-complex-not-to-scale-The-ac fig3_267375476` (2011), [Online; retrieved 13.02.2026]

[25] O. Brüning, H. Burkhardt, S. Myers, *The Large Hadron Collider*, Prog. Part. Nucl. Phys. **67(3)**, 705 (2012)

[26] S. e. Chatrchyan (CMS), *The CMS experiment at the CERN LHC*, JINST **3**, S08004 (2008), also published by CERN Geneva in 2010, URL `https://cds.cern.ch/record/1129810`

[27] *High Luminosity LHC Project*, `https://hilumilhc.web.cern.ch/content/hl-lhc-project` (2026), [Online; retrieved 01.03.2026]

[28] *ATLAS ITk Pixel Detector Overview*, `https://cds.cern.ch/record/2922777/files/ATL-ITK-SLIDE-2024-659.pdf?version=1` (2025), [Online; retrieved 01.03.2026]

[29] *Technical Design Report: A High-Granularity Timing Detector for the ATLAS Phase-II Upgrade*, Technical report, CERN, CERN-LHCC-2020-007, ATLAS-TDR-031, Geneva (2020), URL `https://cds.cern.ch/record/2719855`

A. Appendix

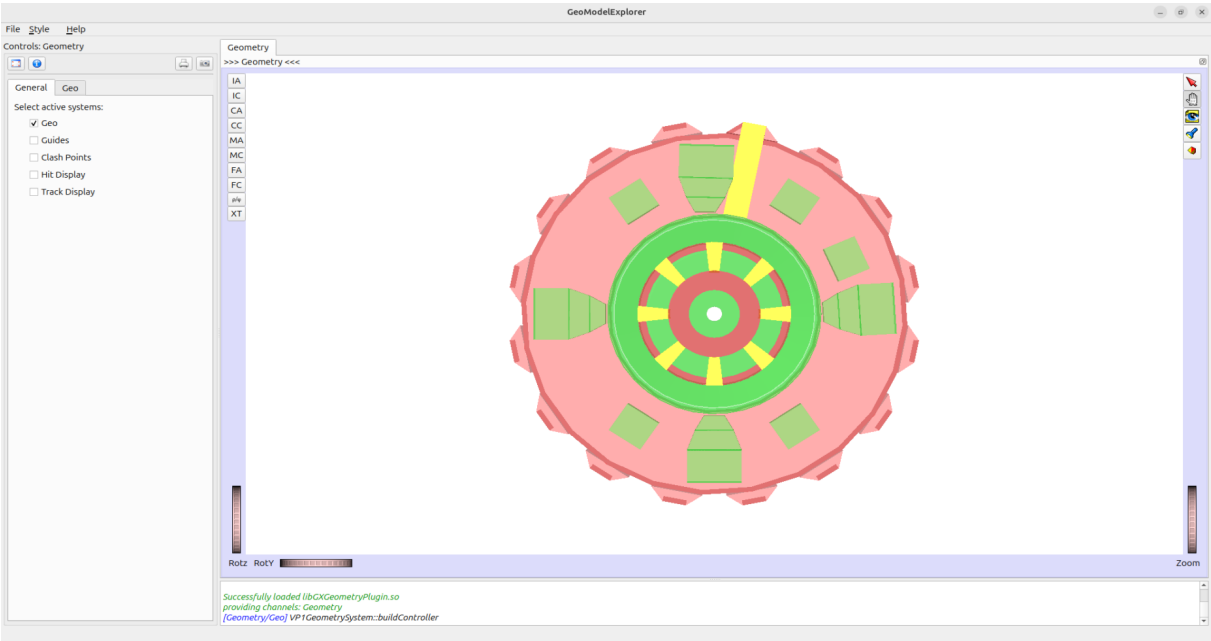

Figure A.1.: The GeomodelVisualisation tool overlay shown comes with many features to visualize the geometry and to include clashpoints into the visualisation as well. This overlay was used to make all the visualisations of the GeoModelXML based model in this thesis.

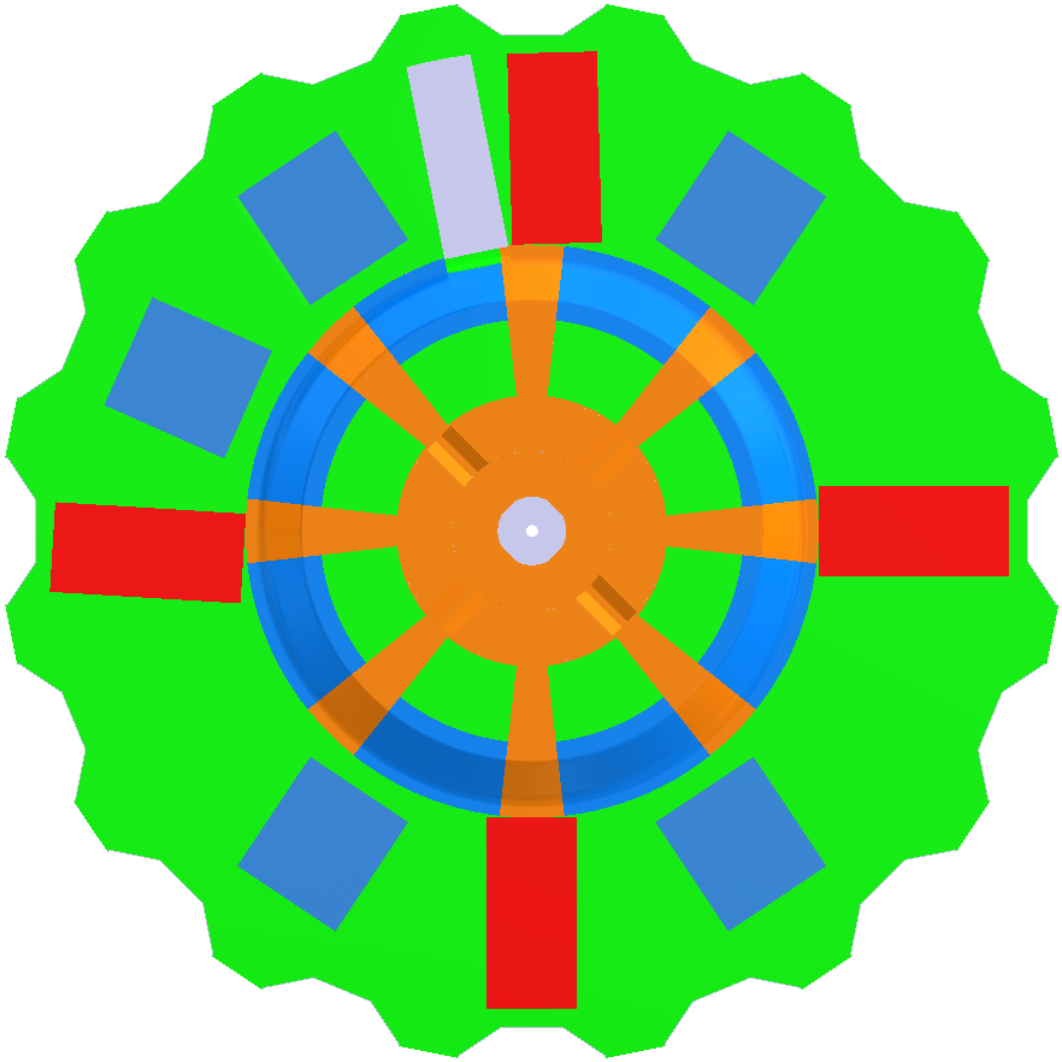

Figure A.2.: The IEM (A side) seen from the inside of the ITk detector. All of the optoboxes in red and splitterboxes in blue sit on top of the sealplate. The outer green volume is the structural sealplate and the housing for cables, pipes and the boxes. The inner parts are all subvolumes of the bulkhead which encompasses cables, pipes and connectors. The model serves as a guideline for the envelopes of the Crack barrel region, not the technical details. An asymmetry is shown on the top, left of the optobox in red, which is a box that houses cables.

Figure A.3.: The side view of the IEM shows the space between the A and C side where the ITk is positioned. The endcaps are beyond the CBR. This side view shows the protrusions and profile of the CBR.

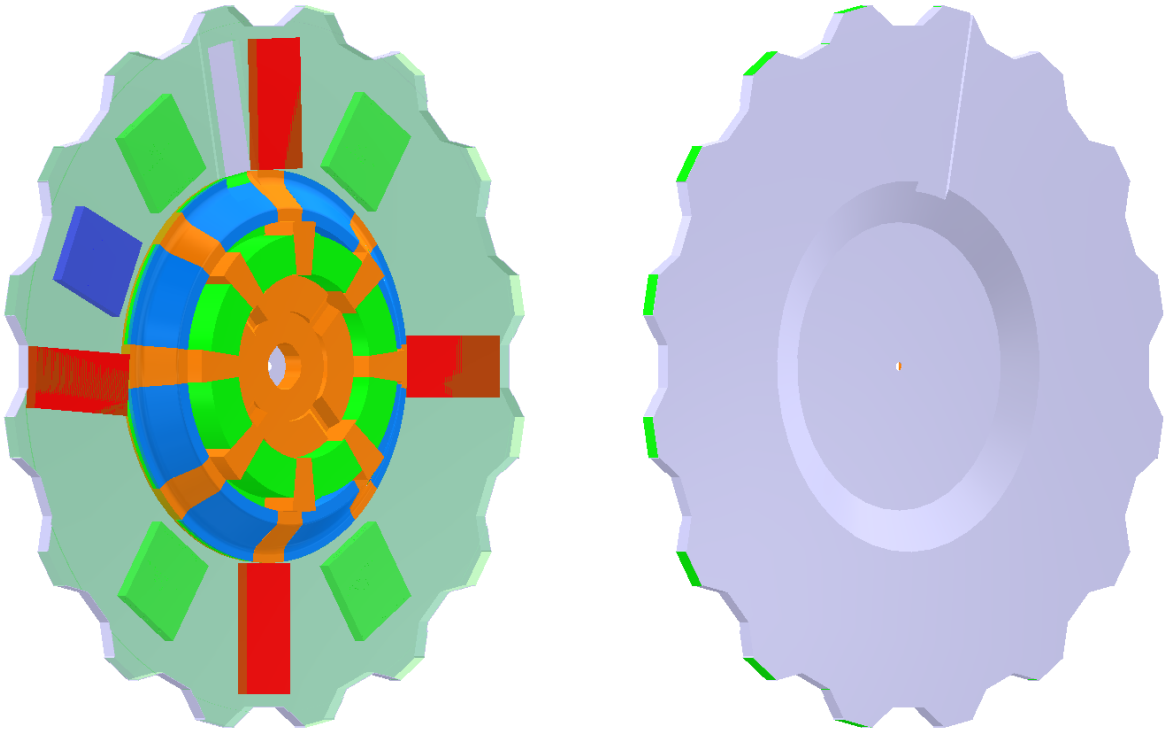

Figure A.4.: The IEM shown on an angle to better visualize the front and back view as well as the protrusions into the ITk barrel. The left side sealplate is made transparent in order to show the splitterboxes and optoboxes which are hidden inside. The splitterboxes for the strip detector are shown in green and the splitterbox for the pixel detector is shown in blue to differentiate. On the back side shown on the right on can observe the rounded edges and the slope inwards which mimic cables and pipes running there as tightly as possible.

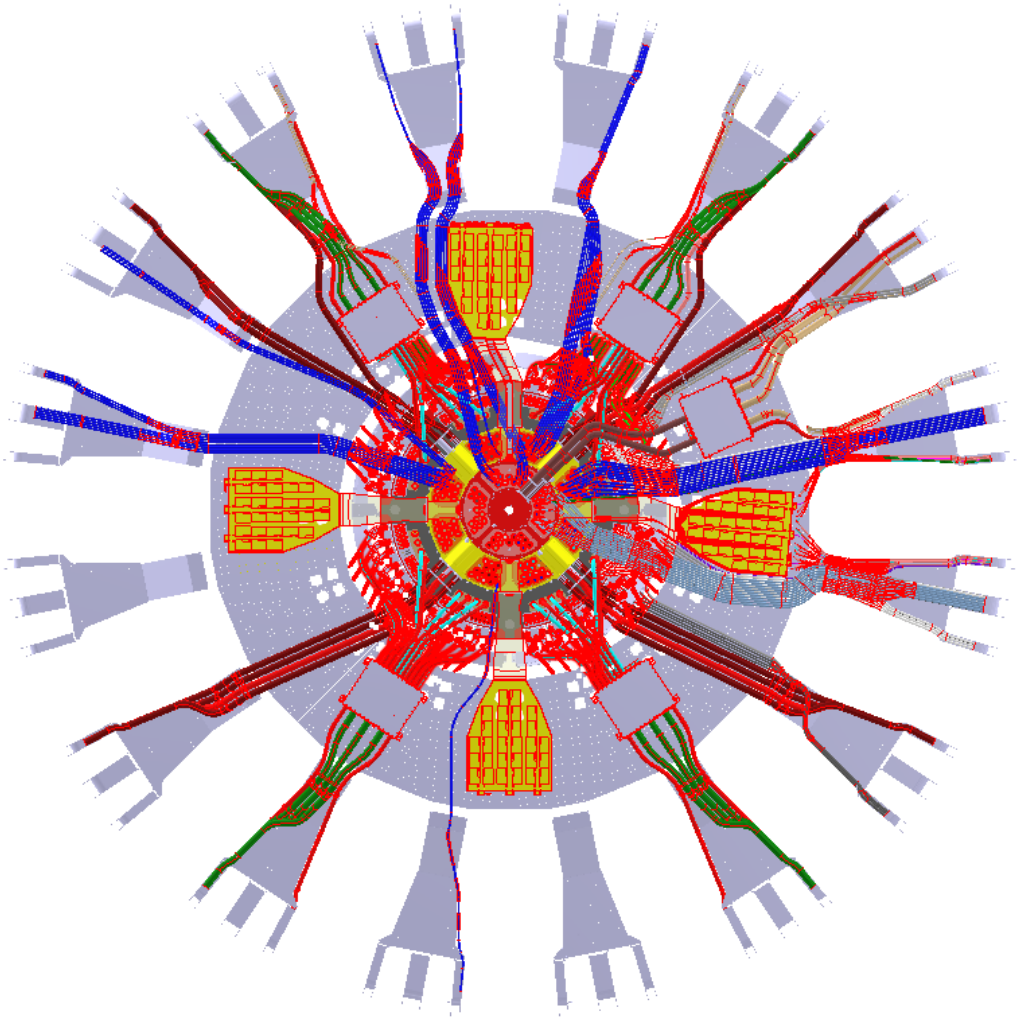

Figure A.5.: The ISM seen from inside the ITk barrel. This model shows differently shaped optoboxes in yellow and splitterboxes in gray with a red outline compared to the IEM. Also the sealplates' inner radius differs slightly which corresponds to a smaller bulkhead section in the middle that is made up of a lot of cables and pipes. Additionally to the CBR further cables and connectors are shown on the outside, past the outer radius of the sealplate. This model includes all technical detail needed to build the detector and is too complex to be used in simulation, but useful to get crucial information about the geometry.

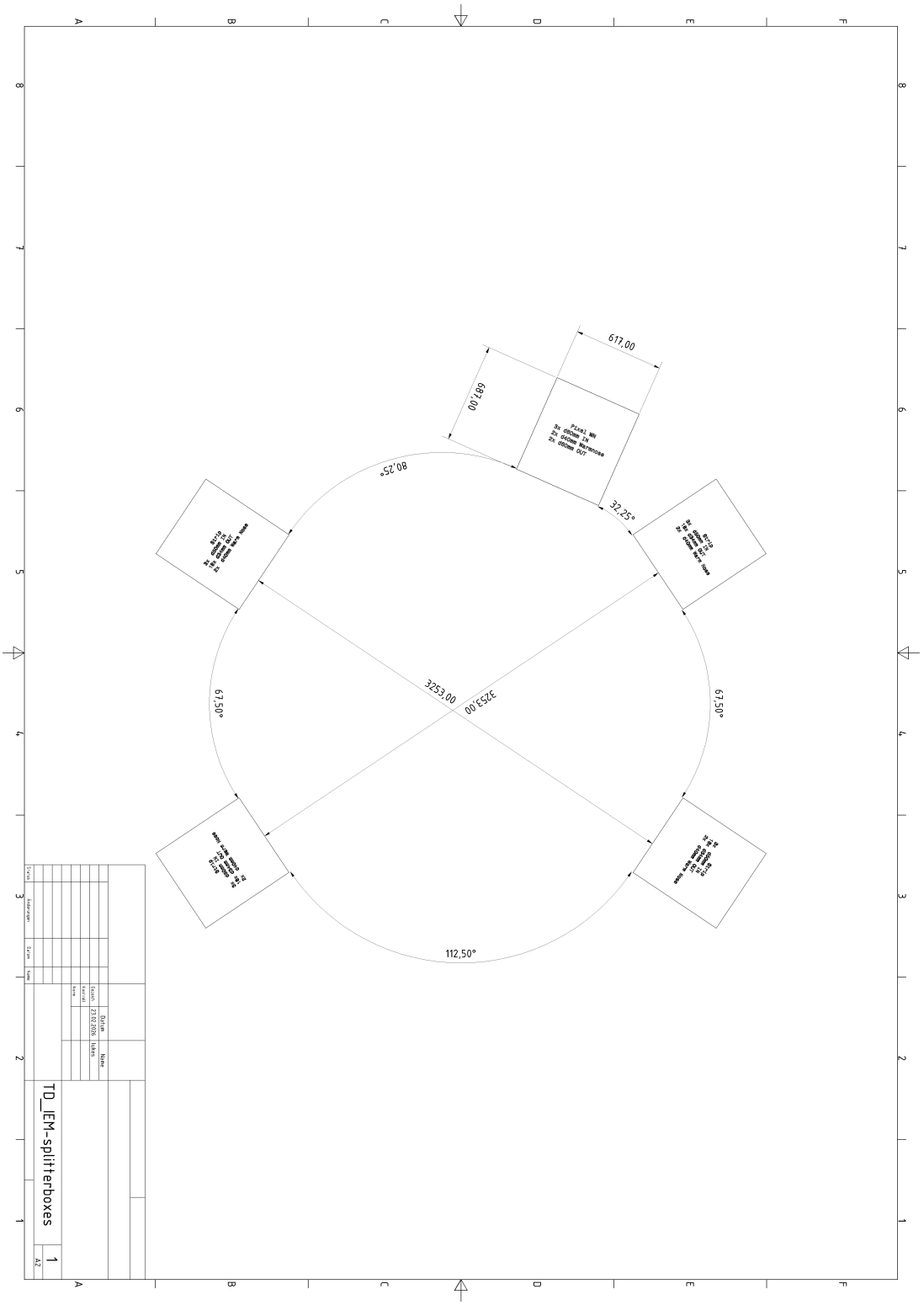

Figure A.6.: Technical drawing of the splitterboxes on the A side (C side is the equivalent, but mirrored), created from the ITk Envelope Model.

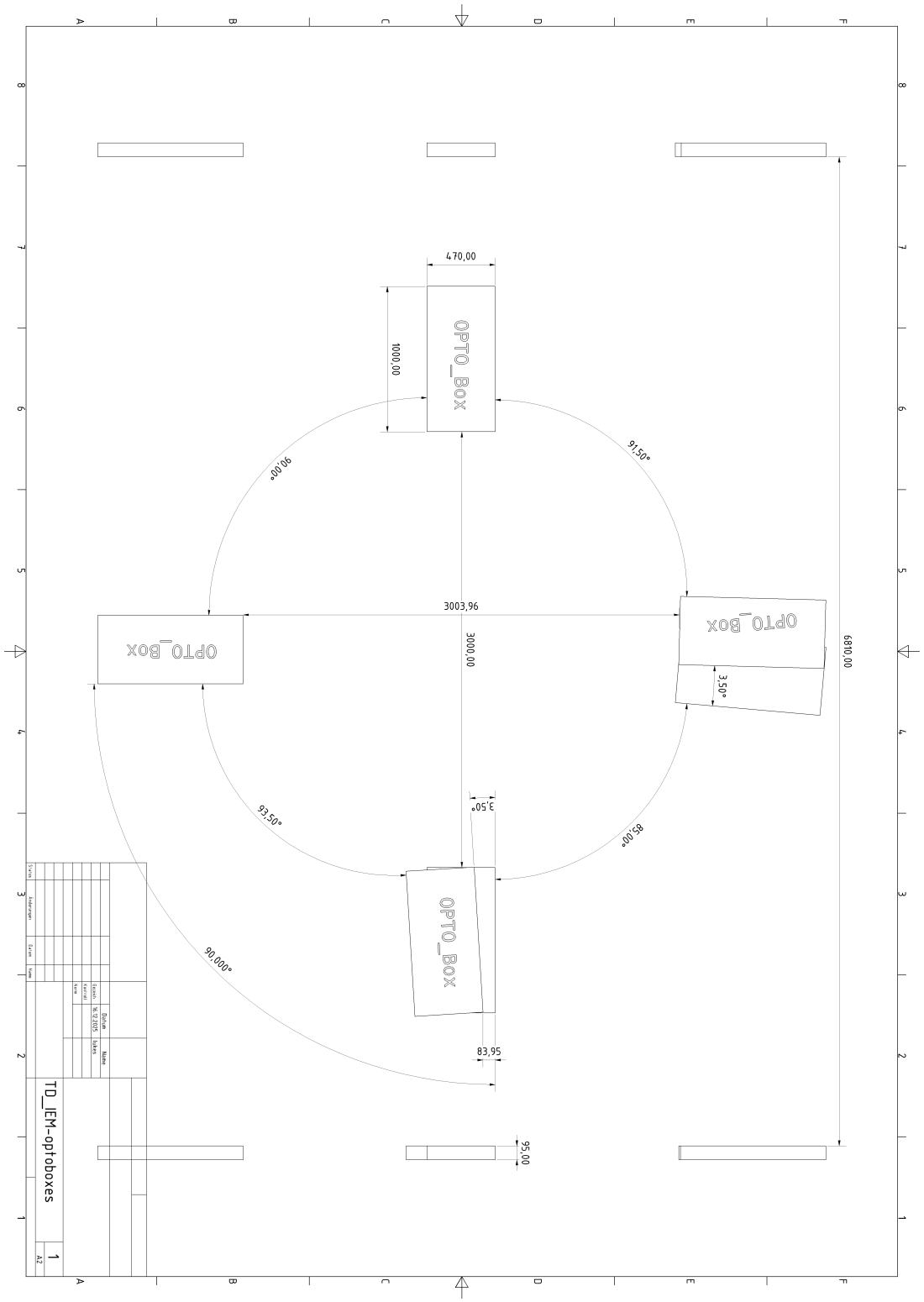

Figure A.7.: Technical drawing of the optoboxes on the A (front) and C (back) side, created from the ITk Envelope Model.

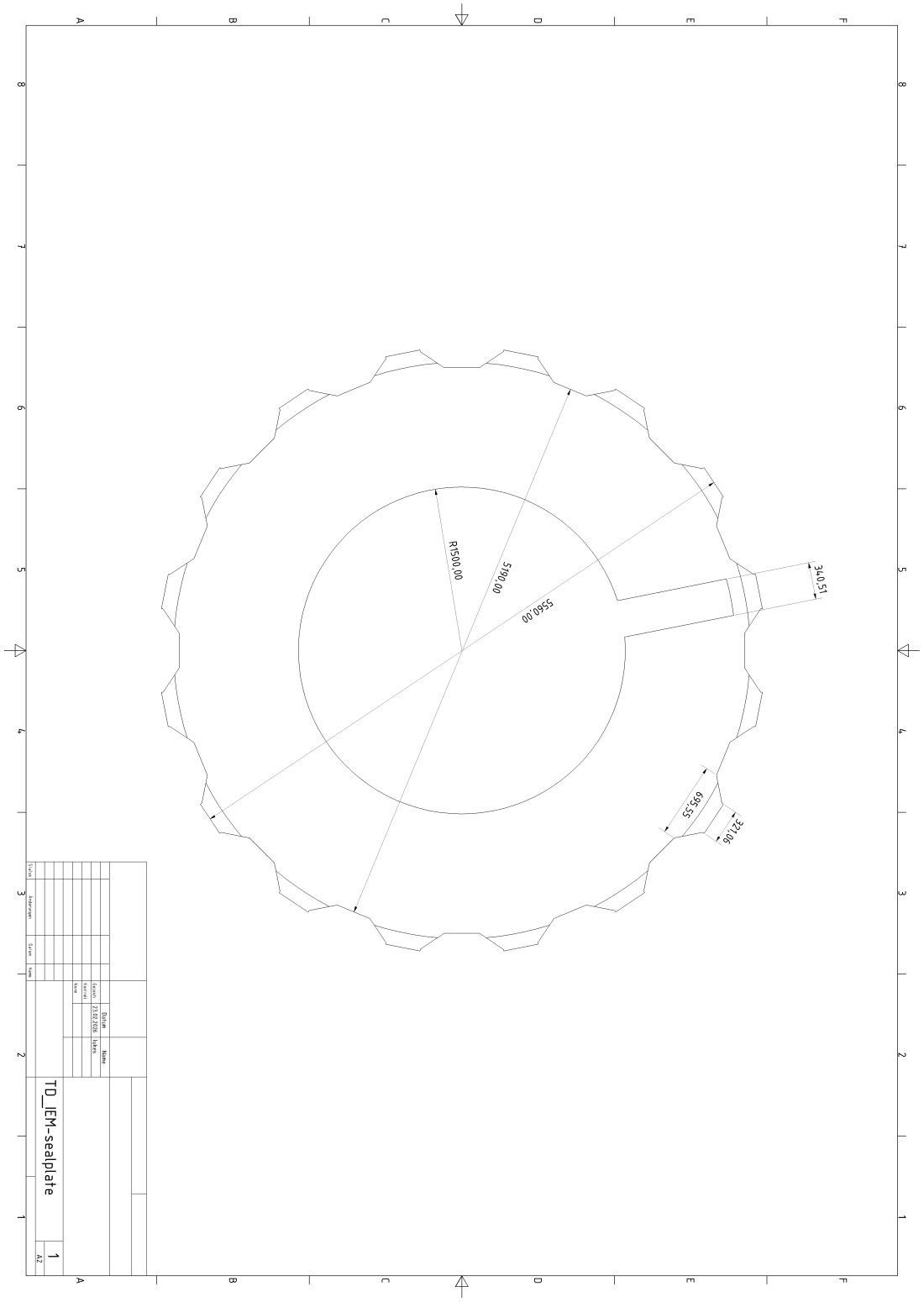

Figure A.8.: Technical drawing of the sealplate, created from the ITk Envelope Model.

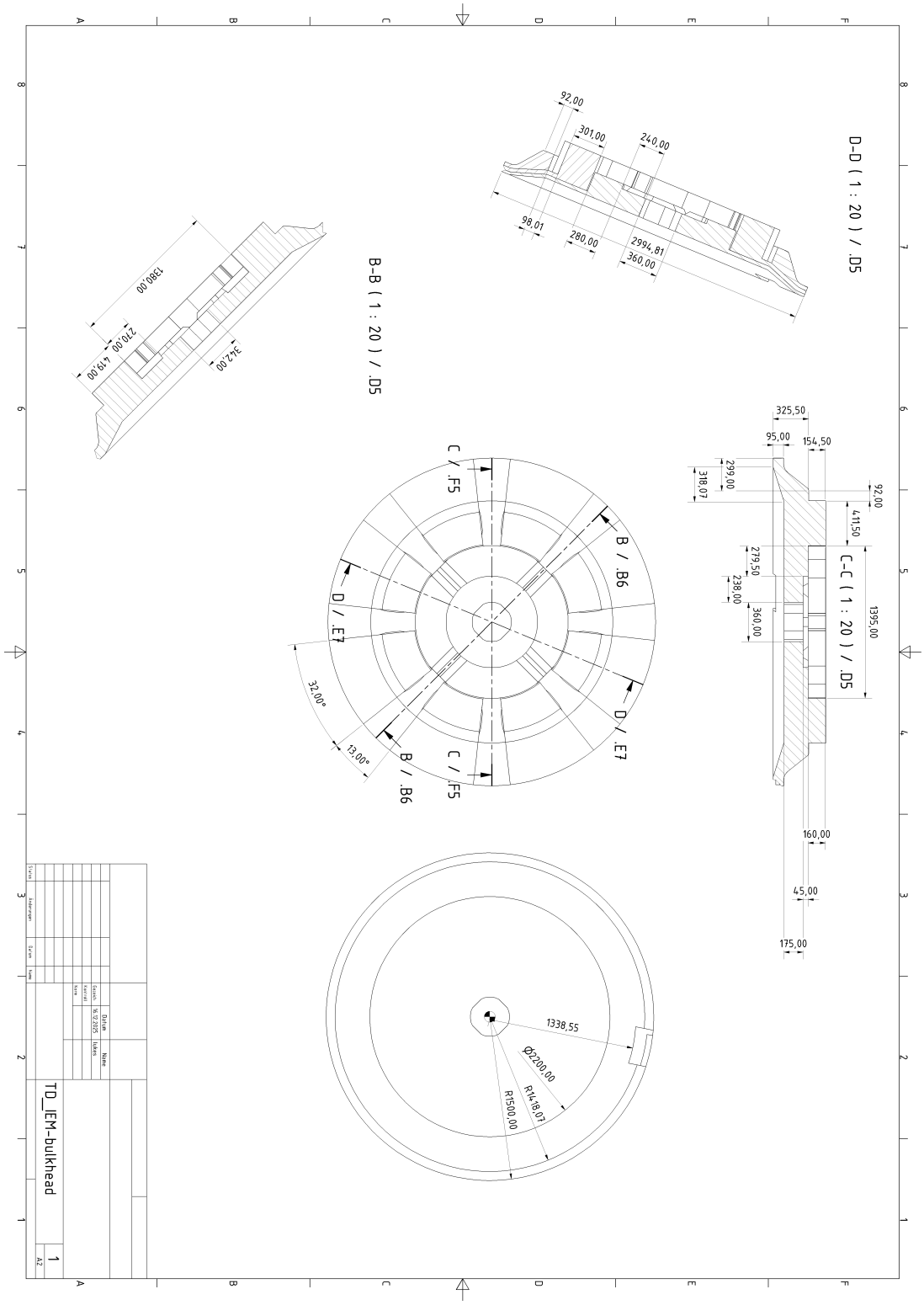

Figure A.9.: Technical drawing of the bulkhead, created from the ITk Envelope Model.

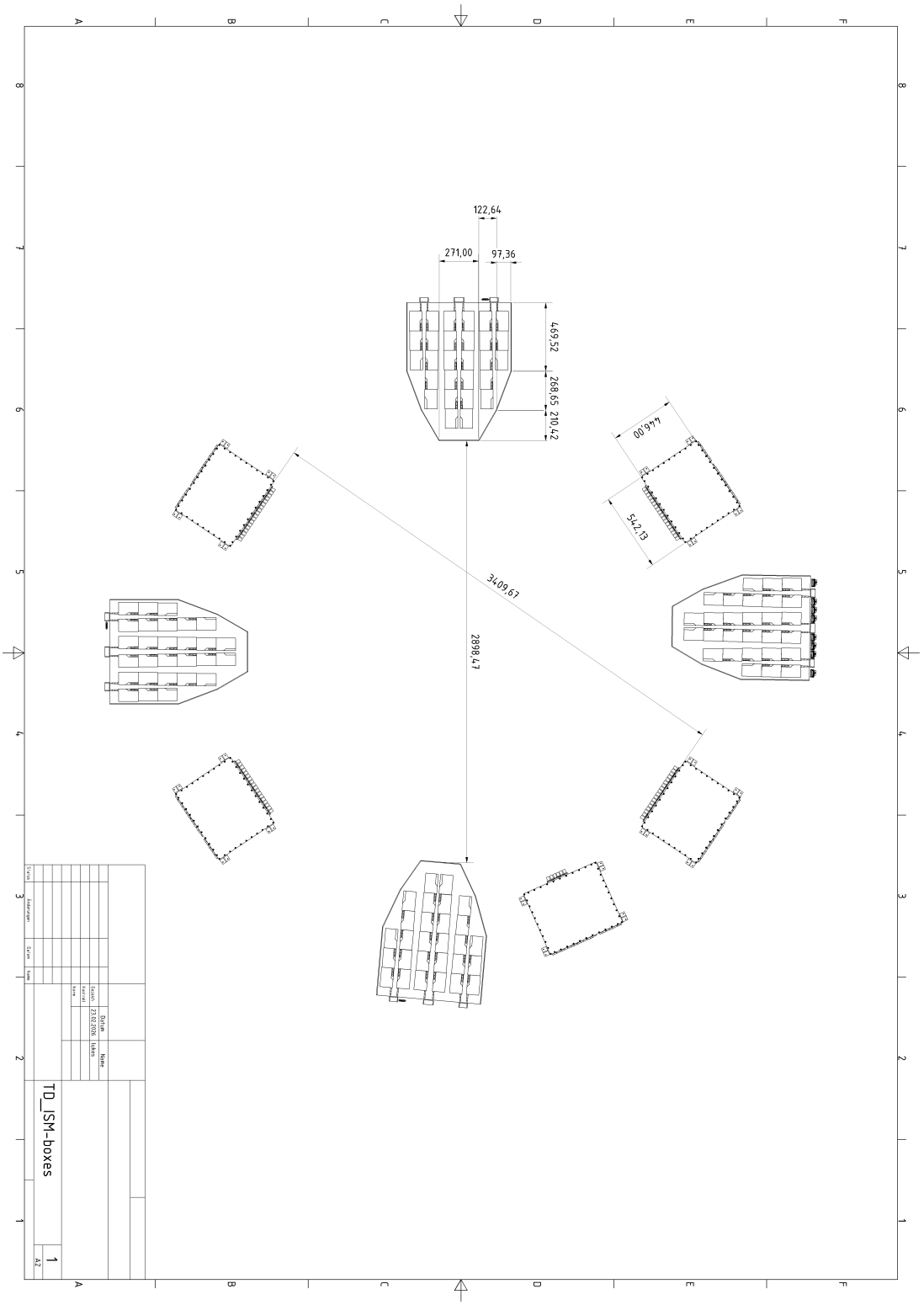

Figure A.10.: Technical drawing of the optoboxes and splitterboxes on the A side, created from the ITk Services Model.

Danksagung

Eine wissenschaftliche Arbeit wie diese schreiben zu können, ist nur durch die Hilfe von vielen anderen Personen möglich, denen ich hier meinen herzlichen Dank aussprechen möchte.

Vielen Dank an alle Personen im II. Physikalischen Institut, die mich fachlich sowie auch menschlich auf dieser Reise begleitet haben. Insbesondere danke ich Prof. Stan Lai und Anne Gaa, denen ich für die fantastische Planung, wöchentliches Feedback, ununterbrochene Unterstützung und eine tolle erste Erfahrung in der wissenschaftlichen Arbeit danken möchte. Ein Dank gebührt auch allen, mit denen ich ausserhalb des II. Physikalischen Instituts zusammenarbeiten durfte und die mich mit Informationen und Feedback unterstützt haben.

Ebenso möchte ich mich bei meinen Eltern und meinem Bruder bedanken, die mich bei allem was ich tue unterstützen und immer für mich da sind.

Erklärung nach §13(9) der Prüfungsordnung für den Bachelor-Studiengang Physik und den Master-Studiengang Physik an der Universität Göttingen:
Hiermit erkläre ich, dass ich diese Abschlussarbeit selbständig verfasst habe, keine anderen als die angegebenen Quellen und Hilfsmittel benutzt habe und alle Stellen, die wörtlich oder sinngemäß aus veröffentlichten Schriften entnommen wurden, als solche kenntlich gemacht habe.
Darüberhinaus erkläre ich, dass diese Abschlussarbeit nicht, auch nicht auszugsweise, im Rahmen einer nichtbestandenen Prüfung an dieser oder einer anderen Hochschule eingereicht wurde.

Göttingen, den 11. Mai 2026

(Luke Selzer)